Study of rare processes induced by 209-GeV muons

W. H. Smith,* A. R. Clark, K. J. Johnson, L. T. Kerth, S. C. Loken,
T. W. Markiewicz, P. D. Meyers, M. Strovink, and W. A. Wenzel

*Physics Department and Lawrence Berkeley Laboratory,
University of California, Berkeley, California 94720*

R. P. Johnson, C. Moore, M. Mugge, and R. E. Shafer

Fermi National Accelerator Laboratory, Batavia, Illinois 60510

G. D. Gollin,† F. C. Shoemaker, and P. Surko‡

Joseph Henry Laboratories, Princeton University, Princeton, New Jersey 08544

(Received 14 October 1981)

Analysis of dimuon final states from 1.4×10^{11} positive and 2.9×10^{10} negative 209-GeV muons in a magnetized iron calorimeter has set a lower limit of 9 GeV/c^2 on the mass of a heavy neutral muon (M^0), and a 90%-confidence-level upper limit of $\sigma(\mu N \rightarrow b\bar{b}X)B(b\bar{b} \rightarrow \mu X) < 2.9 \times 10^{-36}$ cm^2 for the production of bottom hadrons by muons. The dimuon mass spectrum from 102 678 trimuon final states places a 90%-confidence-level upper limit for the muoproduction of Υ states: $\sigma(\mu N \rightarrow \mu \Upsilon X) B(\Upsilon \rightarrow \mu^+ \mu^-) < 22 \times 10^{-39}$ cm^2. In addition, analysis of 71 rare multimuon events, including four- and five-muon final states, is presented.

I. INTRODUCTION

Much of particle physics appears to be described by gauge theories. The standard model[1] is based on the group $SU(3) \times SU(2) \times U(1)$, spontaneously broken into $SU(3)_c \times U(1)_{EM}$. This theory was elaborated by the work of Glashow, Illiopoulos, and Maiani,[2] which introduced charmed hadrons. This, in turn, was naturally extended by Kobayashi and Maskawa[3] to three left-handed doublets of quarks, which allowed the incorporation of the τ lepton and its neutrino and the new bottom quark which comprises the Υ family.[4] If this model is to form the bulwark of our understanding of the structure of matter, then it must be comprehensively studied.

This exploration may proceed down several avenues. One can look for currents which have not been seen, but which have not been experimentally ruled out. A current of this type is a right-handed weak current coupling the muon to a neutral heavy muon. Another route is to study the interactions of the newly discovered quark to see if it behaves in a manner analogous to the lighter and better studied quarks. The experimental study of hadrons with bottom quarks is just beginning. The primary experimental evidence involves the detection of the direct leptons from semileptonic decays

of bottom mesons.[5] A third approach is to look for rare or "exotic" phenomena. A rich source of such phenomena is multimuon final states. There have been reports of "super" neutrino-induced trimuon events at Fermilab,[6] which are not consistent with the conventional physics usually employed to explain these trimuons. In addition, experiments at CERN[7] and Fermilab[8] have observed neutrino-induced four-lepton events for which an adequate explanation is lacking.

A particularly fertile ground for the exploration of these areas is muon physics. The right-handed chirality of a high-energy muon beam provides a unique probe of the right-handed weak current. As a source of virtual photons, the muon beam can explore the behavior of heavy-quark states in kinematic regions inaccessible through other means. Finally, by taking advantage of the ability of muons to penetrate vast quantities of matter, one can use massive targets to conduct searches for rare processes with cross sections as low as 10^{-39} cm^2.

For these purposes, a Fermilab muon experiment, E203/391, was performed to study a broad range of muon-induced physics. The Berkeley-Fermilab-Princeton multimuon spectrometer was designed to have a high sensitivity to any number of muons in the final state. A large solid-iron

magnet integral with the target provided uniform acceptance over the entire length of the apparatus. The experiment was unique in its ability to do multimuon physics because of its full acceptance over its entire fiducial region, due to the lack of any insensitive area in the vicinity of the muon beam.

This paper presents results from data taken with the multimuon spectrometer. Sections II and III describe the experiment and its analysis. Section IV presents a search for heavy neutral muons. Sections V and VI detail limits on the muoproduction and virtual photoproduction of bound- and open-bottom-quark states. Section VII shows the analysis of the sample of 71 rare multimuon final states.

II. THE EXPERIMENT

A. The muon beam

The muon beam was produced by the decay in flight of pions and kaons produced by the 400-GeV proton beam incident on a 30-cm aluminum target. Figure 1 shows a schematic diagram of the Fermilab muon beam. A series of quadrupole magnets, labeled $Q1$, focused the secondaries from

the target into a 400-m-long decay pipe. Momentum selection was accomplished by bending the beam to the right with dipole $D1$ and then to the left with dipole $D2$. The currents in these dipoles were set to select a particle of one sign and a momentum near 215 GeV/c. The momentum acceptance was 2.5%. The 60 feet of polyethylene absorber in dipole $D3$ stopped hadrons in the beam. Quadrupole $Q4$ focused the beam on the apparatus, while dipole $D4$ bent the beam into the Chicago cyclotron magnet (CCM) for targeting on the spectrometer.

Figure 2 shows the beam line and its monitoring from the focusing quadrupoles to the multimuon spectrometer. Hodoscopes and proportional wire chambers before and after the dipole magnets and the Chicago cyclotron magnet identified beam particles and provided momentum measurements. Multiple Coulomb scattering of muons in the polyethylene and muons scraping the beam elements produced halo muons in the muon laboratory. Several veto counters and a large veto wall identified these halo muons. The number of muons in the halo was roughly equivalent to the number of muons in the beam. The muon beam produced intensities up to 6×10^6 muons/spill in the beam area, which was 8 in. high by 13.5 in. wide at the front of the spectrometer. The yield of total beam muons per proton was as high as 4×10^{-7}.

B. Multimuon spectrometer

A schematic view of the multimuon spectrometer is shown in Fig. 3. It is composed of 91 plates of steel 4 in. thick and 8 ft square. Each plate has two slots cut in it through which two coils running
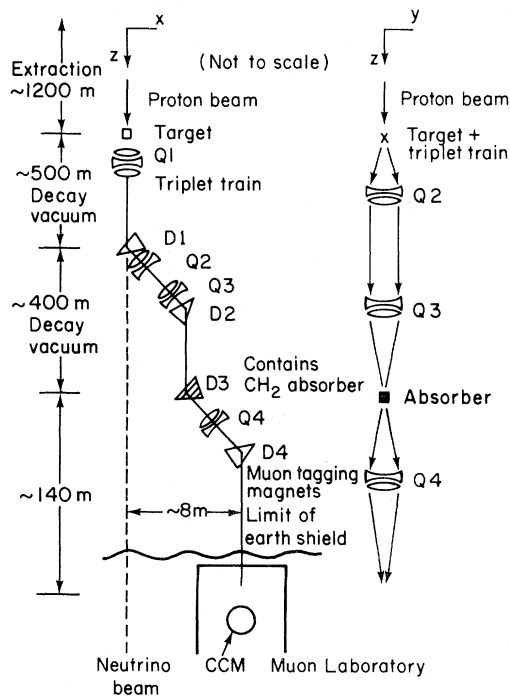

FIG. 1. Schematic diagram of the Fermilab muon beam from the extracted proton beam through the Chicago cyclotron magnet (CCM), just upstream of the multimuon spectrometer.
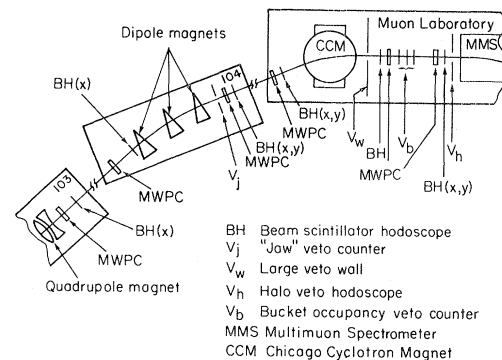

FIG. 2. Detailed view of the beam magnets, proportional chambers, and scintillation counters along the muon beam in enclosures 103 and 104 and in the muon laboratory.
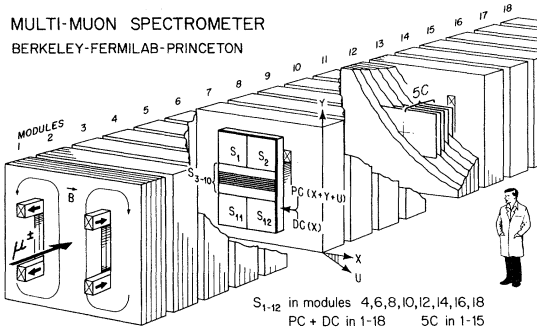
FIG. 3. Schematic view of the apparatus. $S_1 - S_{12}$ are trigger scintillators (1 of 8 banks). DC and PC are 1 of 19 pairs of drift and proportional chambers. Each proportional chamber measures projections on three coordinates. The scintillators labeled $5C$ are 5 of 75 counters performing hadron-shower calorimetry.

the length of the spectrometer were placed. The fiducial area, located between the coil slots, was magnetized to a total 19.7 kG vertical field, which was uniform to 3% over the central 1.4×1 m^2 area of each slab.

The steel slabs were distributed with one lone plate in front followed by groupings of five slabs, called modules. An individual module is shown in Fig. 4. Modules were separated from each other by a 10-in. gap. The first slab and the slabs in the first 15 modules served as the target with a density

of 6.1 kg/cm^2. The steel also served as a hadron and photon filter with an average density in the spectrometer of 4.7 g/cm^3. Particles were required to traverse 4 modules, almost 12 absorption lengths, before identification as muons.

Three types of magnetic measurements were made to determine the magnetic field in the multi-muon spectrometer. Flux-loop measurements determined the absolute normalization for the field integrals in the various modules. These were done with wire loops around the steel plates that measured the induced emf as the magnet was ramped on and off. Search coil measurements in the gaps between iron slabs determined the relative field shape as a function of x and y. Finally, various physical measurements necessary to calculate the field integral were performed, such as determining the width of iron in each module. The field was mapped with 0.2% accuracy in the central area of the spectrometer. The polarity of the field was reversed periodically.

Hadron showers produced in interactions were sampled every 10 cm by plastic calorimeter scintillation counters placed after every slab in the first 15 modules. The calibration of the calorimeter was obtained by statistical comparison with the magnetic measurement of the energy lost in an interaction (subtracting the outgoing muon energies from the energy of the incoming muon). The rms accuracy of the hadron calorimetry was ΔE
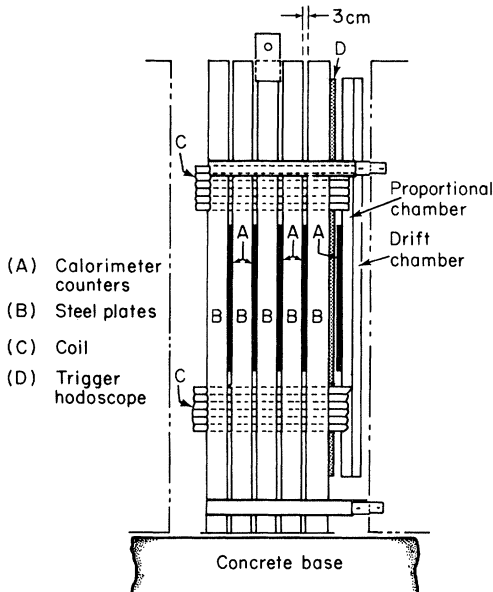

FIG. 4. Side view of one module containing five steel plates followed by five calorimeter counters and the trigger scintillator bank, proportional chamber, and drift chamber in the large gap that separates the groups of five plates.
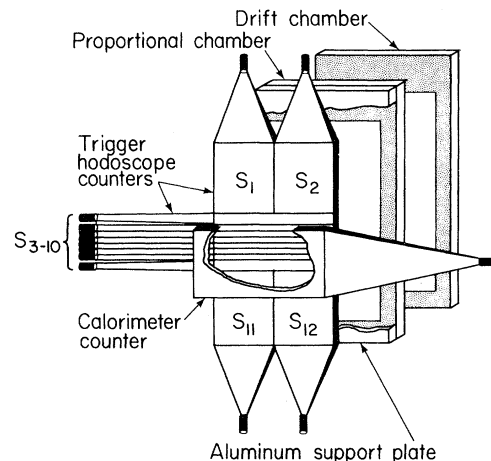

FIG. 5. An exploded view of the detectors within a typical gap between magnet modules. The trigger hodoscope follows the calorimeter counter. Counters S_1, S_2, S_{11}, and S_{12} are "paddles" 20.75 in. wide and 23.8 in. high. Counters $S_3 - S_{10}$ are "staves." S_3 and S_{10} are 41.5 in. wide and 5.98 in. high while $S_4 - S_9$ are 41.5 in. wide and 1.55 in. high.

$= 1/5E^{1/2}$ for ΔE and E in GeV, with a minimum uncertainty of 2.5 GeV. A detailed description of the calorimeter uniformity and calibration is found in Refs. 10 and 49.

After every even-numbered module, beginning with the fourth, banks of scintillation trigger counts were installed. The configuration of these counters is shown in Fig. 5. They consist of four large paddle counters at the top and bottom, and six narrow staves in the middle, framed by two wider staves.

C. Wire chambers

A multiwire proportional chamber was placed after every module and the single slab at the front. The proportional chambers had three planes of wires. There were 336 anode wires spaced at 3 mm which read out coordinates in the horizontal (x), or bend-plane, direction. Coordinates in the diagonal (u) and vertical (y) directions were registered by means of 5-mm-wide cathode strips composed of four high-voltage wires apiece. The u coordinate made a 30° angle with the x coordinate. The diagonal plane consisted of 176 such strips and the vertical 192. Each strip was connected to one input of a differential amplifier as shown in Fig. 6. Although spread over many cathode strips, the induced charge produced a count only in the one or two electronics channels closest to the peak, even when the pulse height far exceeded threshold. This center-finding circuitry gave a pulse-pair resolution better than that achievable with conventional circuitry.[49] The separation between the diagonal and vertical cathode planes and the anode plane was 1 cm. The chambers were active over the entire fiducial area 1.8 m high by 1.1 m wide.

The resolution of the anode-plane (x) measurements was 1 mm and the resolution of the

FIG. 6. The network of differential amplifiers sensing the center of the charge distribution induced on the proportional-chamber cathode strips.

cathode-plane $(u$ and $y)$ measurements was 3 mm. Outside the beam region the anode and cathode planes had efficiencies of 95 and 94%, respectively. In the central beam region at the highest beam intensities, these efficiencies for the most upstream chambers could drop as low as 83 and 59%. Generally, chambers would have efficiencies down to 88% for the anode plane and 76% for the cathode planes in the central beam region at highest beam flux. Data from the chambers were read out for 70 nsec during a trigger.

Attached to every multiwire proportional chamber was a single drift-chamber plane with 56 vertical wires measuring coordinates in the bend plane. The drift cell width was $\frac{3}{4}$ inch and the distance from the sense wires to the field-shaping high-voltage plane was $\frac{1}{8}$ inch. Each drift chamber covered the entire fiducial area. The drift chambers were gated for 250 nsec during a trigger. The resolution of each drift chamber was 250 μm and their average efficiency was $>98\%$. The drift chambers provided the maximum resolution compatible with multiple Coulomb scattering in the bend plane in order to produce more precise muon momentum determination. The drift-chamber system is described in detail in Ref. 9.

D. Triggers

The apparatus ran with four simultaneous triggers: "beam," "one muon," "two muon," and "three muon." The beam trigger required a muon to trigger in the beam hodoscope counters upstream of the spectrometer without any of the halo veto counters firing. This trigger was always used in coincidence with all other triggers and provided a trigger by itself when prescaled by 3×10^5. The one-muon trigger was used to detect high-Q^2 muon scattering and therefore required each of three consecutive trigger banks to have a hit in a paddle counter and to have no hits in any stave.

The two-muon trigger required three trigger banks to have ≥ 2 hits and at least 20 GeV of energy deposited in the calorimeter. In addition, the hits in the most downstream contributing trigger bank were required to be nonadjacent. This trigger is described in detail in Ref. 10. The three-muon trigger required three consecutive trigger banks to have ≥ 3 hits, but did not involve the calorimeter. It also demanded that one of the hits be nonadjacent to the other two hits in the most downstream two trigger banks. The rates of the one-, two-, and three-muon triggers relative to one beam muon were 3×10^{-6}, 8×10^{-6}, and 1.2×10^{-5}, respectively.
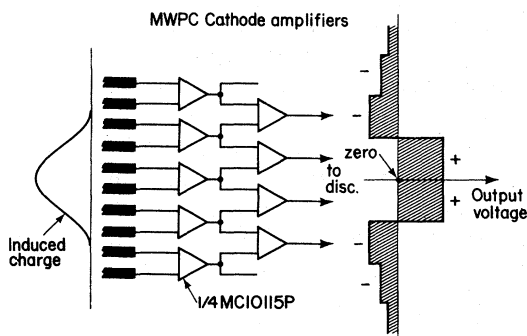
III. ANALYSIS

A. Track finding

The track-finding program combines contiguous proportional-chamber hits into single hits with measurement errors equal to $1/\sqrt{12}$ the distance between the first unstruck wires on either side of the group of wire hits. If a diagonal (u) plane wire is struck within 0.75 cm of a hit-x-wire and hit-y-wire crossing, the x, y, and u hits are declared a matched triplet. The program begins at the back of the spectrometer and requires three triplets or two triplets and unmatched x and y hits in a third chamber. The three chambers containing these hits must not be separated from each other by more than one empty chamber.

The track is extended one chamber at a time. At each chamber a new triplet or unmatched hits are attached, the trajectory is recalculated and a projection of the track is extended into the next chamber where a window for searching for new hits is opened. This procedure continues until the track finder passes two contiguous chambers where the search window containing no hits or the location along the beam (z) axis of the event vertex determined by calorimetry is reached.

B. Calorimeter vertex

There are two methods of searching for the location of the event vertex along the beam axis by examining the pulse heights in the calorimeter counters. In the case of a one-muon or two-muon trigger, or a three-muon trigger accompanied by more than 40 GeV of energy deposited in the calorimeter, an "inelastic" calorimeter vertex is found. In the other cases, an "elastic" calorimeter vertex is found. If the inelastic vertex finder fails on a three-muon trigger, the elastic vertex finder is used. In all other cases, if the vertex finder fails the vertex is set at the front of the spectrometer so as not to interfere with track finding. Pictures of an inelastic and an elastic event are found in Figs. 17 and 19, respectively.

The elastic calorimeter vertex finder computes the likelihood of the vertex in each steel plate using normalized one- and three-particle calorimeter distributions. The routine uses the pulse heights from all the calorimeter scintillators in the calculation and searches from the first plate to the plate before the most downstream trigger-scintillator bank contributing to the event trigger. The inelastic calorimeter vertex finder searches for the calorimeter counter with the largest pulse height.

It then computes for each slab the difference between the number of upstream counters with less than and with greater than 8% of this pulse height. The vertex is assigned to the slab with the maximum value of this difference.

C. Beam track finding

The information from the wire chambers, shown in Fig. 2, along the muon beam lines in enclosures 103, 104, and the area upstream of the multimuon spectrometer in the muon laboratory is used with the first proportional chamber in the spectrometer to determine the slope, position, momentum, and their errors for the incident beam muon at this first chamber. The momentum is measured from the bend of the dipoles in enclosure 104 and the Chicago cyclotron magnet in the upstream end of the muon laboratory. If the χ^2 for this fit is poor, the chamber contributing the largest residual is discarded and the track is refit.

Irrespective of its χ^2, the fitted muon trajectory is then projected into the spectrometer, one chamber at a time, and triplets or, if there are none, unmatched hits are assigned to the track. The trajectory is then refit using the new chamber hits and projected into the next chamber. The procedure continues until the calorimeter vertex is reached, or in the case of a failed calorimeter vertex in the first slab, until the most downstream trigger bank contributing to the event trigger.

After all track finding is complete, the two drift-chamber hits closest to the fitted proportional-chamber trajectory in the x view are attached to every track. The choice of which of these hits, if any, to incorporate in the track is made by the track-fitting routine.

D. Track fitting

The track-fitting program begins with the track provided by the track-finding program. At first, only proportional-chamber tracks are fitted. Once a track has been fit in the bending plane, the program scans the drift-chamber track arrays and replaces proportional-chamber hits with chosen drift-chamber hits if they lie within a distance equal to three times the uncertainty in the position of the fitted track. The combined drift- and proportional-chamber hits are then fitted by the momentum-fitting routine again.

E. Momentum-fitting routine

For outgoing tracks, the momentum-fitting routine takes as input a point along the z axis for ref-

erence and all the proportional- and drift-chamber hits downstream of that point. It makes a simultaneous fit to the free parameters describing the muon tracks. In the bending plane, these are the transverse position x_0 and direction tangent s_0 of the muon at the reference point and the muon momentum $p = 1/\rho_0$, projected in that plane.

N additional free parameters d_j are introduced equal to the projected transverse-momentum impulse due to multiple Coulomb scattering in each of the N magnet segments that the muon traverses after the reference point. A magnet segment is defined as the steel between the n wire chambers that contain a muon track hit located at x_i. Thus, there are N additional measurements d_j with variances e_j, where e_j is the rms value of d_j appropriate to the thickness of the iron segment. When the d_j are introduced, σ_i, the errors on the x_i, become deviations due only to intrinsic chamber measurement error.

Each magnet segment imparts an impulse h_j of transverse momentum to the muon. The h_j were corrected for departure from normal incidence. In addition, the measured coordinate X_i was given a correction ΔX_i for the effect of muon energy loss in each magnet segment. Each iteration of the fit changed these ΔX_i appropriately, based on the last best-fit momentum. Hence the full χ^2 is

$$\chi^2 = \sum_{i=1}^{n} \frac{x_i - (X_i + \Delta X_i)^2}{\sigma_i^2} + \sum_{j=1}^{N} \frac{d_j^2}{e_j^2} \, ,$$

where

$$x_i = x_0 + s_0 z_i + \sum_{j=1}^{N} (z_i - w_j)(h_j \rho_0 - d_j \rho_j) \, ,$$

$$\Delta X_i = \sum_{\substack{j=1 \\ w_j < z_i}}^{N} (z_i - w_j) h_j \Delta \rho_j$$

and where z_i and w_j are the coordinates along the beam axis relative to the reference point of the measurement planes and magnet segment midpoints, and $\rho_j = \rho_0 + \Delta \rho_j$, where $\Delta \rho_j$ is produced by the energy loss in the iron.

The best fit to the free parameters x_0, s_0, ρ_0, and $(d_1, \ldots, d_N)$ was obtained by solving the $N + 3$ simultaneous linear equations

$$\frac{\partial \chi^2}{\partial x_0} = \frac{\partial \chi^2}{\partial s_0} = \frac{\partial \chi^2}{\partial \rho_0} = \frac{\partial \chi^2}{\partial d_1} = \cdots = \frac{\partial \chi^2}{\partial d_N} = 0 \, .$$

For the nonbending plane fit (y coordinate) to an outgoing track the momentum is taken from the x fit and is not a free parameter. For incoming beam tracks fit in the spectrometer, the incident momentum and direction in the x and y views are taken from a fit made to the beam system.

If the momentum is being fitted as a free parameter, then the routine iterates using as input to the fit a value of the momentum that is a function of the previous guessed input values and output values returned by the routine. For all tracks and views, if the χ^2 of the fit track is unsatisfactory the routine removes the measurement plane whose hit contributes the largest amount to the χ^2 and refits the tracks. No more than $\frac{1}{3}$ of a track's hits may be removed and a minimum of five hits must remain. In the bending view each measurement plane may contain two drift-chamber hits and one proportional-chamber hit for each track. The fitting routine tries swapping the chosen hit for another before it removes the measurement plane. The fit rms momentum resolution is 8%.

F. Vertex finding

In preparation for vertex finding, the routine eliminates tracks that penetrated but were not detected by the trigger counters. These tracks are due to muons out of time with the event by more than the 19-nsec rf-bucket interval. Tracks that were mistakenly broken into two or more segments by the track-finder program are rejoined by composing a new track from hits in the segments. Tracks are selected for rejoining on the basis of the number of hits they have in common and the angle they make with each other at their point of contact or closest approach. The decision to merge tracks is based on the χ^2 of a fit made to a track composed of the combined hits of both tracks. Single tracks that the track finder reconstructed as two tracks have one of the duplicates removed.

Finally, tracks with over five blank measurement planes between their apparent termination and their fit exit from the spectrometer in either the x or y view are eliminated. The event is thrown out if no secondary tracks remain, or, in the case of a two-muon or three-muon trigger, if less than two secondary tracks remain. These are events which accidently triggered as having two or more secondary tracks when these tracks did not actually occur in the event.

The vertex finder first chooses the secondary tracks to be used in determining the vertex on the basis of their distance of closest approach to the beam track, the error in this distance, the χ^2 of their original fit and the distance they extend

upstream of their point of closest approach. The z position of the vertex, zv, and its error, σ_{zv}, are then chosen by a weighted average of the included tracks' closest points of approach and the calorimeter vertex if the χ^2 per degree of freedom of the fit including it with the track vertex is less than 3.

The vertex finder scans $5\sigma_{zv}$ on either side of zv in 10-cm steps, using the fits of the included tracks, the beam track, and their errors to determine the most likely point (x_0, y_0) in common for all these tracks at each step. A χ^2 is determined for each point, where, given a step in z, the index runs over the included tracks:

$$\chi^2 = \sum_i \frac{(x_i - x_0)^2}{(\Delta x_i^2 + \Delta x_0^2)} + \frac{(y_i - y_0)^2}{(\Delta y_i^2 + \Delta y_0^2)} \ .$$

The minimum χ^2 determines the z position of the vertex. The vertex finder then performs a 1-cm scan in a 20-cm range centered on this vertex, finds a new best vertex and finally performs a $\frac{1}{3}$-cm scan in a 2-cm range centered on this vertex.

During vertex-finding procedures the calorimeter vertex is examined for consistency with the track vertex. The calorimeter vertex is considered consistent if it is within a distance, equal to 1.5 times the uncertainty in its position, away from the vertex determined by the tracks and calorimeter vertex combined. If it is found consistent, it is included with its error in the χ^2 scan. If it is not, it is removed and the vertex finding begins again without it. If the inelastic calorimeter vertex is available, then the vertex finder does a 1-cm scan in a 100-cm range centered on the calorimeter vertex and is not allowed to discard the calorimeter vertex. The $\frac{1}{3}$-cm scan follows as before. If the overall χ^2 for the vertex is unsatisfactory, the routine attempts to throw one or more tracks out of the set of included tracks and repeats the entire procedure.

Once this vertex has been determined, it is attached to all tracks and they are refit by the momentum-fitting routine. If any track except the beam track has a large χ^2 from this fit, its original fit is restored and it is considered excluded from the vertex. The severity of the χ^2 cut is adjusted to provide a sample of at least three outgoing tracks or two outgoing tracks and an inelastic calorimeter vertex to be attached. However, a track is never included in the vertex if its χ^2 per degree of freedom exceeds 7.5 in either the x or y view when the vertex is attached.

If it is found that the sample of tracks attached to the vertex is not the same as that used in previously determining the vertex, or that any measurement planes were removed in the momentum fit with the vertex attached that were included in the original momentum fit, the tracks are all refitted without the vertex attached, but will all the newly removed measurement planes on each track removed *a priori*. The entire vertex-scanning and -determining procedure is then repeated. If it is found that the use of an inelastic calorimeter vertex resulted in too large a χ^2, the vertex-finding and -fitting procedure is repeated with the calorimeter vertex treated as though it were an elastic vertex. Once the new vertex has been determined, all these tracks are once again fitted with this vertex included as one of their hits and they are constrained to go through it.

G. Acceptance modeling

Monte Carlo calculations of the detector acceptance are based on a standard program onto which the various physics generators are coupled. These generators include the muoproduction of neutral heavy muons, ψ's, Υ's, pions, kaons, charmed mesons, and bottom mesons. The Monte Carlo program uses a sample of real beam muon events to simulate the real beam distribution. These beam muons are propagated through the spectrometer to the interaction vertex.

The daughter muons from the generator are propagated until they leave the spectrometer. This propagation includes energy loss from μ-e collisions, muon bremsstrahlung, and electron pair production. It also calculates the bending of muon trajectories in the magnetic field and includes multiple Coulomb scattering. Large-angle scattering is parameterized by a nuclear form factor. A basic attempt is also made to model the hadronic shower spread through the chambers. The Monte Carlo program also produces calorimeter pulse heights and trigger-counter latches. Interactions that trigger the apparatus are written on tape using the same format employed in actual data taking.

IV. LOWER LIMIT ON NEUTRAL-HEAVY-MUON MASS

A. Experimental and theoretical background

Considerable speculation has been devoted to the possible existence of heavy neutral gauge leptons. Variations of the standard $SU(2) \times U(1)$ model[11] have been proposed where the known lepton doub-

lets are coupled to a neutral heavy lepton,[12] and where both right- and left-handed doublets exist and include M^0's.[13] Reference 14 presents a Konipinski-Mahmoud[15] type lepton assignment including two new neutral leptons. References 16 and 17 discuss a minimal extension of the SU(2)×U(1) gauge model that includes an isodoublet of heavy leptons. Reference 18 presents an SU(3)×U(1) model involving an M^0. Grand unification schemes frequently introduce M^0's, e.g., those[19] which embed $SU(2)_L \times U(1)$ in $SU(3)_L \times SU(3)_R$. In addition to the M^0, heavy doubly charged gauge muons (M^{++}) have been proposed in the context of an extended SU(2)×U(1) theory in doublets with the known singly charged leptons.[12]

There exist few experimental limits on the masses of heavy muons. Studies of π and K decay[20] exclude the M^0 mass from the range $m_\mu < m_{M^0} < m_K$. A bubble-chamber study of ν_μ-N interactions[21] sets a 90%-confidence lower limit of 1.8 GeV/c^2 on the mass of the heavy muon M^-. Although there are 90%-confidence lower limits of 2.4 GeV/c^2 from ν_e-N scattering[22] and 8.4 GeV/c^2 from ν_μ-Fe interactions[23] on the M^+ mass, there is no further experimental constraint on the M^0 mass.

Possible evidence for M^0 production has arisen from three experiments. Two $\mu^- e^+$ events produced by ν_μ-N interactions below 30 GeV in the SKAT bubble chamber[24] were attributed[25] to the production of an M^0 with $1.4 < m_{M^0} < 2.4$ GeV/c^2. Other attempts have been made to explain these events as M^0 production[26] with an extended model of SU(2)×U(1), or in the framework of the Gürsey-Sikivie[27] gauge model based on either the E(6) or E(7) gauge group.[28] However, no corroborating evidence for the M^0 has resulted from the study[29] of ν- and $\bar{\nu}$-induced μe pairs. In a cosmic-ray experiment[30] deep underground, five events were interpreted either as evidence for a heavy lepton with mass 2−4 GeV/c^2 or as the cascade[31] of a new charged heavy lepton to an M^0. However, two subsequent searches[32] found no such events. Originally the observation of neutrino-induced trimuon events at Fermilab[33] prompted their interpretation[34] as examples of M^0 production. Further experiments and analyses found this phenomenon to be compatible with conventional processes: heavy lepton production could account for no more than 10−20% of these events.[35]

B. Rate calculation

We have calculated the expected rates for $\bar{M}^0$ and M^{++} production in this experiment, assuming the incident muon to be coupled with Fermi strength to the M by means of a right-handed weak current. The right-handed coupling, present in most models containing a heavy gauge lepton, is compatible with our experimental conditions due to the $\sim 80\%$ left-handed polarization of the μ^+ beam.[36] In the limit of negligible muon mass, invariance to weak-isospin rotation gives $\sigma(\mu^-(\mathrm{LH})N \rightarrow \nu_\mu X) = \sigma(\nu_\mu N \rightarrow \mu^- X)$, where LH refers to the left-handed muon helicity and N is an average of protons and neutrons. Also, for negligible M^0 mass, $\sigma(\mu^-(\mathrm{LH})N \rightarrow M^0 X) = (g_L/g)^2 \times \sigma(\mu^-(\mathrm{LH})N \rightarrow \nu_\mu X)$, where $g_L{}^2/g^2$ is the ratio of left-handed coupling strengths for M^0 and ν_μ. Finally, $\sigma(\mu^+(\mathrm{LH})N \rightarrow \bar{M}^0 X) = (g_R/g_L)^2 \times \sigma(\mu^-(\mathrm{LH})N \rightarrow M^0 X)$, where $g_R{}^2/g_L{}^2$ is the ratio of abnormal-helicity to normal-helicity weak-coupling strengths[37] for the M^0. For a right-handed current of Fermi strength $g_R = g$. Except for effects of finite lepton mass, these equations combine to give $\sigma(\mu^+(\mathrm{LH}) N \rightarrow \bar{M}^0 X) = (g_R/g)^2 \times \sigma(\nu_\mu N \rightarrow \mu^- X)$.

Using the simplest parton model with the interaction of a leptonic and hadronic current via a single vector particle (W^+) exchange,[38] invoking the Callan-Gross relation,[39] neglecting terms of $O(m_{M^0}/E_\mu)$, and considering only $\Delta S = \Delta C = 0$ processes and isoscalar targets,

$$\frac{d^2\sigma(\mu^+(\mathrm{LH})N \rightarrow \bar{M}^0 X)}{dv\,dy} = \left[\frac{g_R}{g}\right]^2 \frac{G^2 E m_N F_2(x)}{\pi y},$$

where $v = xy = Q^2/s$, $(1-y)$ is the fraction of the laboratory muon energy retained by the $\bar{M}^0$, and $F_2(x) = 18 v W_2{}^{\gamma N}(x)/5$. We parametrize $v W_2{}^{\gamma p}$ as in Ref. 40 and set[41] $v W_2{}^{\gamma n} = (1 - 3/4x)v W_2{}^{\gamma p}$, giving for an iron target $v W_2{}^{\gamma N} = (1 - 0.4x)v W_2{}^{\gamma p}$. The differential cross section is independent of $\bar{M}^0$ mass, except for kinematic restriction of the allowed area of the $Q^2 - v$ plane.

The differential decay rate for $\bar{M}^0 \rightarrow \mu^+ \bar{\nu}_\mu$, where the $\bar{M}^0$ is coupled to the μ^+ by a $(V+A)$ current, is

$$\frac{d^5\Gamma(\bar{M}^0 \rightarrow \mu^+ \mu^- \bar{\nu})}{dx_- dx_\nu d\phi_\nu d\cos\theta_\nu d\phi_-}$$

$$\propto x_\nu (1 - x_\nu)(1 - h\cos\theta_\nu).$$

In the $\bar{M}^0$ rest frame $x_-(x_\nu)$ is $2p/m_{M^0}$ for the $\mu^-(\bar{\nu}_\mu)$, θ_ν and ϕ_ν define the $\bar{\nu}_\mu$ direction relative to the $\bar{M}^0$ direction, ϕ_- defines the μ^- direction relative to the $\bar{\nu}_\mu$ direction, and h is the $\bar{M}^0$ helicity. Since the $\bar{M}^0$ carries the left-handed polarization of the incident μ^+, the two muons are emitted pre-

ferentially forward and together carry an average of 80% of the $\overline{M}^0$ energy in the laboratory. This direction of polarization is optimal for apparatus acceptance and background rejection.

C. Results

Monte Carlo events have been generated according to the above formulas at lepton masses of 1, 2, 3, 5, 9, 12, and 14 GeV/c^2. Simulated $\overline{M}^0$ and M^{++} events at each mass are binned in $(Q^2)^{1/2}$ and in $p_\perp$, the daughter-muon momentum transverse to Q. For this analysis, Q^2 is defined by taking the highest-energy beam-sign final-state muon to be a scattered beam muon. The $\overline{M}^0$ (M^{++}) Monte Carlo events are compared to data events containing exactly two opposite- (same-) sign reconstructed final-state muons. The data events consist of 76 350 opposite-sign and 46 615 same-sign dimuon final states produced by 1.4×10^{11} positive and 2.9×10^{10} negative 209-GeV muons.

Kinematic cuts were chosen individually for each heavy lepton type and mass in order to exclude data while retaining Monte Carlo $\overline{M}^0$ and M^{++} events. Primarily, these cuts demand a particular range of invariant mass.[42] In addition, for $m_{M^0} > 3$, > 2, or < 3 GeV/c^2, respectively, the cuts require a 9-GeV minimum outgoing muon energy, a -5-GeV minimum missing energy, or a 50-GeV minimum v. The cuts suppress the principal backgrounds of charm production and π and K decay. An empirical contour then was drawn for each $(Q^2)^{1/2}$-$p_\perp$) plot in order to contain all the data events on the low-$p_\perp$, low-$(Q^2)^{1/2}$ side. The same contour was drawn on the corresponding plot for simulated M events. (If the same contour[43] and cuts, except for the dimuon mass cut, were used for all masses, the limits presented below would rise by a factor of 1.6 on the average.) Figure 7 shows the plots and contour for data and Monte Carlo events corresponding to 6-GeV/c^2 $\overline{M}^0$ production. The Monte Carlo event populations on the high-$p_\perp$, high-$(Q^2)^{1/2}$ side of the contours then provide the cross-section limits.

Figure 8 displays the mass-dependent limits on the product of cross section and $\mu\mu v$ branching ratio (σB) for $\overline{M}^0$ and M^{++} production. Also indicated are the calculated σB for the production of $\overline{M}^0$'s and M^{++}'s, where the branching ratio is assumed to be 0.1 and 0.2 for $\overline{M}^0$ and M^{++}, respectively. At 90% confidence the data exclude the production of a $\overline{M}^0$ or M^{++} coupled with Fermi strength to a right-handed current in the mass range $1 < m_{M^0} < 9$ GeV/c^2. Variations in the

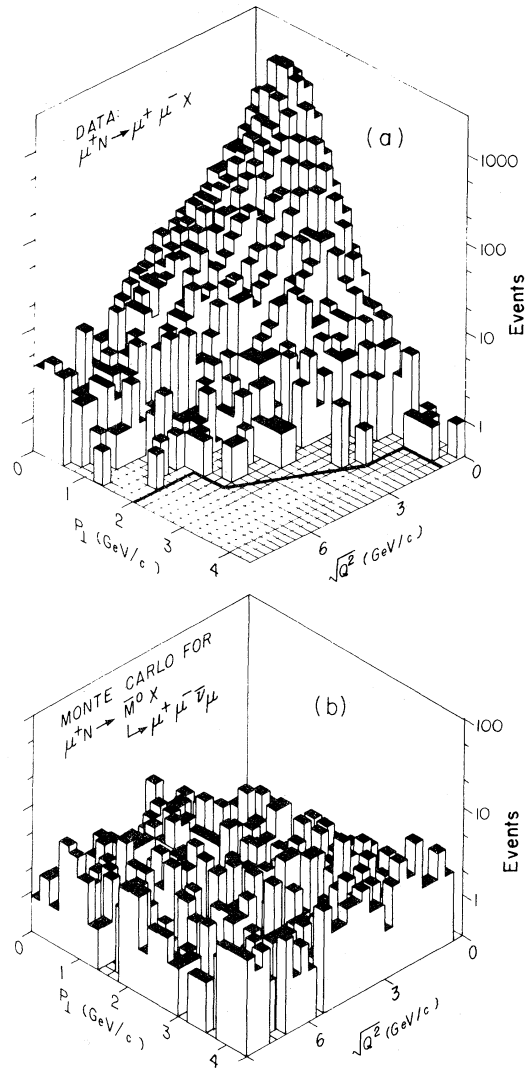FIG. 7. Two-dimensional event distributions versus $\sqrt{Q}$ and $p_\perp$, defined in the text. The vertical scale is logarithmic; bin populations range from 0 to 450. Distribution (a) shows the data and the empirically chosen contour within which these events are contained. Distribution (b) is 77.4$\times$(the simulated population from production and decay of a 6-GeV/c^2 $\overline{M}^0$), with the assumptions described in the text. The events in (b) lying outside the contour in (a) give the quoted σB limit at this mass.

models of heavy-lepton production detailed above relative to the assumed model would result in a different mass limit. Without a special mechanism to suppress pair production, doubly charged leptons in this mass range would have been detected at PETRA. No comparable limits on $\overline{M}^0$ produc-
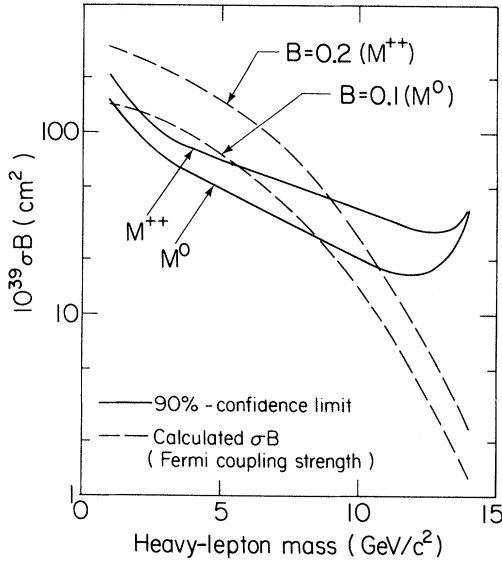
B=0.2 (M^{++})

B=0.1(M^0)

$10^{39}\sigma B$ (cm^2)

100

M^{++}

M^0

10

———90% -confidence limit

— — —Calculated σB
(Fermi coupling strength)

0   5   10   15

Heavy-lepton mass (GeV/c^2)

FIG. 8. Experimental upper limits and calculated cross-section—branching-ratio products σB for heavy-muon ($\overline{M}^0$ and M^{++}) production by 209-GeV muons, plotted versus heavy-muon mass. The calculation assumes $B(M \rightarrow \mu\mu\nu)=0.1(\overline{M}^0)$ or 0.2 (M^{++}), and right-handed coupling of μ^+ to M with Fermi strength ($g_L = g_R$).

tion in this range are available from any other experiment.

V. A LIMIT ON Υ MUOPRODUCTION

The dimuon mass spectrum from an integrated luminosity of 0.78×10^{39} cm^{-2} is derived from 102 678 trimuon final states. This data sample contains 6693 ± 355 examples of J/ψ and ψ' production[44] and contains invariant masses up to 11.5 GeV/c^2. In every event, all three outgoing muons are fully momentum-analyzed and are subjected to an energy-conserving one-constraint fit using calorimetric measurement of the associated shower energy. The quality, statistical power, and range of this sample make it exceptionally suitable for an investigation of the virtual photoproduction of heavy-quark states by muons. At present, there is no other comparable sample from any other experiment. We have chosen here to use the sample to search for muon-induced virtual photoproduction of Υ states.

No limit on Υ production by real or virtual photons has been published. A conference report[45] based on results from the Bologna-CERN-Dubna-

Munich-Saclay (BCDMS) experiment presents the limit $\sigma(\mu N \rightarrow \Upsilon X)B(\Upsilon \rightarrow \mu^+\mu^-) < (6\pm3)\times10^{-39}$ cm^2 (90% confidence) for ~275-GeV muons, where the error is systematic. This limit is based on 761 multimuon events corresponding to an integrated luminosity[45] of 0.7×10^{39} cm^2. A third muon was observed in 11% of these events. No calorimetric information is available. With 48% acceptance for dimuon pairs at the Υ mass, the BCDMS limit corresponds to ≤ 2 Υ candidates (90% confidence). In total, the experiment observed 24 events between 8 and 12 GeV/c^2 in dimuon mass. These were compared to a calculated background of 30 electromagnetic tridents in the same region.

A. Rate calculation

We have calculated the expected Υ rates using a photon-gluon-fusion (γGF) model[46] which accounts[47] for most of the published features[48] of ψ muoproduction. It uses a Bethe-Heitler diagram for heavy-quark production with the nuclear photon replaced by a gluon. Additional soft-gluon exchanges needed to conserve color are assumed not to affect the kinematics. The diagram is shown in Fig. 9. Figures 10 and 11 illustrate the good agreement between the γGF model and ψ production by muons and photons. Using a distribution $G(x)=3(1-x)^5/x$ in gluon momentum fraction x, a bottom-quark mass $m_b=4.7$ GeV/c^2, a bottom-quark charge $|q_b| = \frac{1}{3}$, and a strong coupling constant $\alpha_s = 1.5/\ln(4m_{b\bar{b}}^2)$, where $m_{b\bar{b}}$ is the mass in GeV/c^2 of the produced quark pair, the model predicts Υ muoproduction cross sections of 0.13×10^{-36} cm^2 at 209 GeV and 0.28×10^{-36} cm^2 at 275 GeV. With $B(\Upsilon \rightarrow \mu^+\mu^-)=3.5\pm1.5$ percent,[48] the expected values of $B\sigma$ are $(4.6\pm2.5)\times10^{-36}$ and $(9.8\times4.2)\times10^{-36}$ cm^2, respectively. The BCDMS upper limit is $(60\pm30)\%$ of the latter cross section.

B. Dimuon mass spectrum

Figure 12 displays the spectrum in dimuon mass $M_{\mu^+\mu^-}$ from this experiment. Events below 5 GeV/c^2 in $m_{\mu^+\mu^-}$ are reconstructed and momentum fitted as previously described. Above 5 GeV/c^2, the analysis of all events was checked by a hand reconstruction which was blind to the invariant mass. At all masses the assignment of
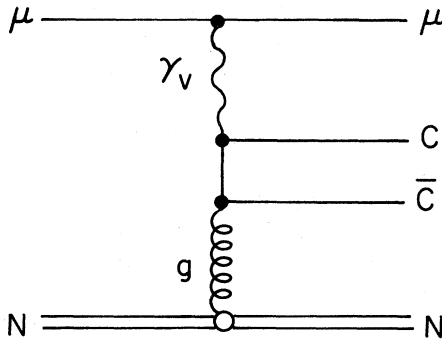
FIG. 9. Feynman diagram for virtual-photon—gluon—fusion production of charm states.

beam-sign secondary muons either to the scattered muon or to the produced muon pair is the critical decision in the analysis. Incorrect pairing of muons from ψ or muon trident production can cause events which properly belong in the low-mass region to be misinterpreted as having a higher mass. Our muon-pairing algorithm was selected primarily to minimize this problem, rather than to maximize correct Υ reconstruction. The scattered muon is chosen to be the one with the smaller value of the square of its scattering angle divided by its scattered energy. Algorithms involving various powers of the scattering angle divided by various powers of the scattered energy were tested on both ψ and Υ Monte Carlo events. The algorithm that was selected minimized the number of ψ Monte Carlo events that were misanalyzed with an invariant mass in the Υ region, while
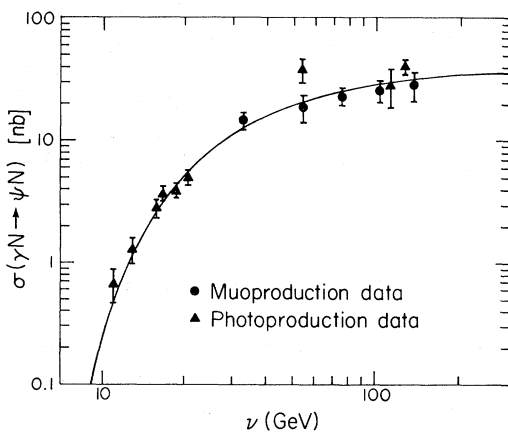

FIG. 10. Theoretical curve corresponding to the photon-gluon cross section compared to $\gamma N \rightarrow \psi N$ data from this experiment (muoproduction data) and from Ref. 53 (photoproduction data). Figure from Ref. 47.
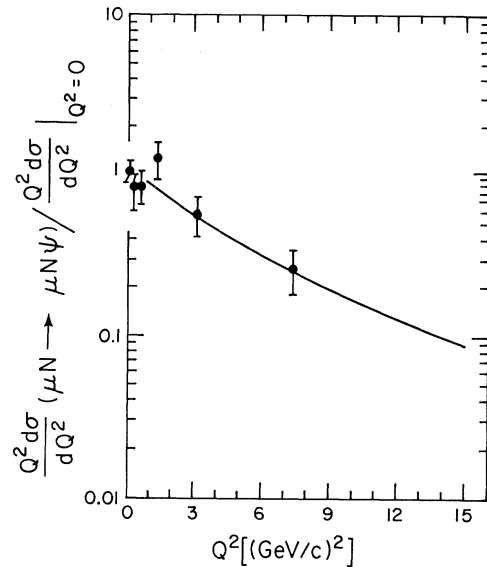

FIG. 11. Theoretical curve corresponding to the photon-gluon cross section compared to ψ muoproduction data from this experiment. Figure from Ref. 47.

maintaining a good throughput of properly analyzed Υ Monte Carlo events. The algorithm is 89% efficient in reconstructing Υ's generated by the Monte Carlo simulation described below. The alternative choice for the scattered muon would produce more than a one-order-of-magnitude exaggeration of the high-mass continuum near the Υ, as shown by the "mispaired" histogram segment in Fig. 12. We emphasize that the muon pairing algorithm can be optimized only if all three final-state muons are momentum-analyzed.

Despite the care exercised in muon pairing, Monte Carlo studies show that there remains a significant contribution in the region $4.7 < M_{\mu^+\mu^-} < 8.4$ GeV/c^2 from incorrectly analyzed lower-mass events. Allowance for these effects is most reliably made by use of an empirical fit to the mass continuum. This mass region, together with the range $1.5 < M_{\mu^+\mu^-} < 2.3$ GeV/c^2, was chosen for the fit in order to exclude regions complicated by charmonium production or rapid variations in low-mass acceptance. The dimuon mass spectrum contains a clear ψ peak which enables the optimization of the trimuon data analysis through its use as a "benchmark." After subtraction of the fit continuum, the ψ peak in Fig. 12 exhibits an 8.5% rms resolution, $\cong 1\%$ larger than the Monte Carlo prediction.[50] The extrapolated continuum contains 1.8 ± 1.0 background events in the Υ region
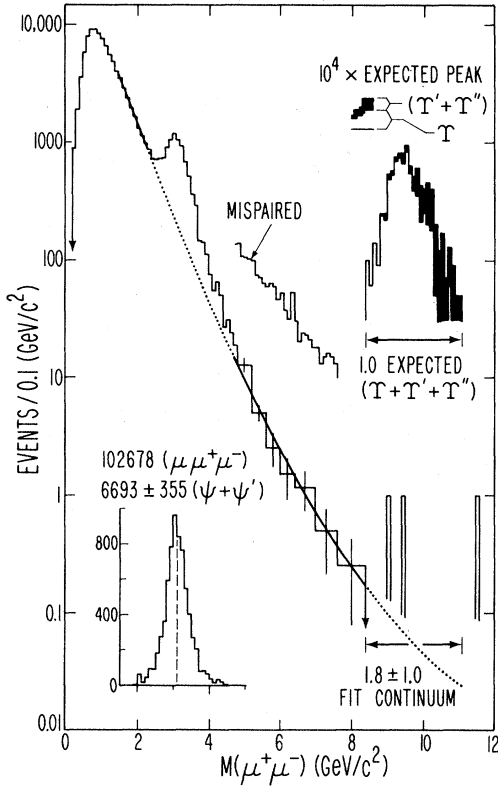
FIG. 12. Spectrum of 102 678 dimuon masses from 75% of the trimuon data. The background is fit by $\exp(a+bm+cm^2)$ in the regions of the solid curve with a χ^2 of 13.7 for 14 degrees of freedom, and is extrapolated along the dotted curve. The "mispaired" histogram segment illustrates the appearance of the mass spectrum if the alternative muon-pairing choice is made. The background-subtracted ψ peak is shown in the lower corner; the expected peak from $10^4\times$(the Monte Carlo—simulated Υ, Υ', and Υ'' sample) is shown in the upper corner, with the contribution from Υ' and Υ'' in black.

$8.4 < M_{\mu^+\mu^-} < 11.1$ GeV/c^2, which in fact includes two observed events. The additional event at 11.5 GeV/c^2 is interpreted as continuum background with 65% probability, or as part of the peak corresponding to known Υ states with 1% probability. With 90% confidence, there are fewer than 3.8 events above the extrapolated background.

C. Acceptance modeling

The Monte Carlo program used to simulate Υ muoproduction is based on a routine which successfully parametrizes our ψ data.[49] In order to

reproduce the experimental ratio of coherent to incoherent ψ production from Fe nuclei, to parametrize threshold effects, and to describe the dependence on $-t$, the square of the four-momentum transferred to the target, the cross section is assumed to be

$$\frac{d\sigma}{dt}(\gamma\mathrm{Fe}\to\psi X)=G(t)\frac{d\sigma}{dt}(\gamma N\to\psi N)(t=0) \ ,$$

$$G(t)=A_e^{\ 2}\exp(\alpha t)+A_e[\,(1-\epsilon\delta)\exp(t)$$
$$+\epsilon\delta\exp(\delta t)]\ .$$

The t resolution of the spectrometer is such that a δ function at $t=0$ is smeared into $\sim\exp(5t)$. Therefore, data from other photon-nucleus experiments[50] are averaged to set the coherent slope α to 150 $(\mathrm{GeV}/c)^{-2}$. The shadowing factor A_e is taken to be $0.9\times(A=55.85)$, based on electron-nucleus scattering data[51] at similar average Q^2. We have used $\beta=3$ $(\mathrm{GeV}/c)^{-2}$, $\delta=1$ $(\mathrm{GeV}/c)^{-2}$ and $\epsilon=1/8$. These choices are consistent with high-energy photoproduction[52] and our experimental t distribution.

The ψ Monte Carlo program is adapted to Υ simulation by appropriately scaling the vector-meson-mass-dependent parameters. Simulated Υ mass-resolution and detection efficiency are 9% (rms) and 22%, respectively. The corresponding values for ψ production are 8.5% (rms) and 19%, showing the uniformity of the experiment over a wide range of dimuon invariant mass. The Υ cross section is normalized to the γGF value described above. Υ, Υ', and Υ'' states are generated in the ratio 1:0.39:0.32 in agreement with recent measurements of $\Gamma_{ee}(\Upsilon):\Gamma_{ee}(\Upsilon'):\Gamma_{ee}(\Upsilon'')$.[53] Υ' and Υ'' production suffer an additional $\sim30\%$ suppression relative to Υ production because of threshold kinematics. The reconstructed peak corresponding to $10^4\times$ the expected signal is shown in Fig. 12; 1.0 events from all Υ states are expected in the data.

D. Results

Our 3.8-event limit, integrated luminosity, and detection efficiency combine to set the 90%-confidence limit[54] $\sigma(\mu N\to\mu\Upsilon X)B(\Upsilon\to\mu^+\mu^-)$ $<22\times10^{-39}$ cm^2. With $B(\Upsilon\to\mu^+\mu^-)$ $=(3.5\pm1.5)\%$,[48] we obtain the 90%-confidence cross-section limit $\sigma(\mu N\to\mu\Upsilon X)<0.78$ $\times10^{-36}$ cm^2, including the error in the branching ratio. This limit lies above published predictions which use either the vector-meson dominance[55,56] or the γGF[57] models. Ignoring any γGF model

uncertainty, this result rules out the choice $|q_b| = \frac{2}{3}$ with 85% confidence. With 67% confidence, the data disfavor the existence of similar bound states of a second charge $\frac{1}{3}$ quark in the Υ mass region.

VI. LIMIT ON BOTTOM-HADRON PRODUCTION

We have examined 36 952 dimuon final states produced by 1.4×10^{11} positive and 2.9×10^{10} negative 209-GeV muons. The majority of these data are due to the muoproduction of charmed hadrons, kaons, and pions, accompanied by their muonic decays. However, it is reasonable to enquire if there might be some contribution to this data from the muoproduction of hadrons containing bottom quarks with the subsequent muonic decay of these hadrons to charmed particles.

We have calculated the expected rate for bottom-meson production using a photon-gluon-fusion (γGF) model, described previously, which accounts for most of the published features[58] of charmed-meson production. Using, as before, a distribution $g(x) = 3(1-x)^5/x$ in gluon momentum fraction x, a bottom-quark mass $m_b = 4.7$ GeV/c^2 and charge $|q_b| = \frac{1}{3}$, and a strong coupling constant $\alpha_s = 1.5/\ln(4m_{b\bar{b}}^2)$, where $m_{b\bar{b}}$ is the mass of the produced quark pair, the model predicts a $b\bar{b}$ muoproduction cross section of 0.93×10^{-36} cm^2 at 209 GeV. If the $b\bar{b} \to \mu X$ branching ratio B is assumed to be 0.17 (essentially the same as that for $c\bar{c} \to \mu X$),[59] the predicted σB is 0.16×10^{-36} cm^2.

A. Monte Carlo calculations

Monte Carlo charm events were simulated by using the γGF model with a charmed-quark mass of 1.5 GeV/c^2 and charge $|q_c| = \frac{2}{3}$. For incoherent events, the same dependence on $-t$, not predicted by the model, was used as for the ψ analysis. Similarly, the same nuclear parameters were used for coherent events. Quark pairs carrying the full photon energy were transformed to D mesons using a fragmentation function[60] $D(z) = (1-z)^{0.4}$ where z is $2\bar{E}_D/m_{c\bar{c}}$ and $\bar{E}_D$ is the D energy in the $c\bar{c}$ rest frame. Charged and neutral D's were produced in a 1:2 ratio[60] and decayed to muons[61] with 4 and 20% branching ratios, respectively.[62] Production and decay of other charmed states was not explicitly simulated. The $K\mu\nu$ ($K^*\mu\nu$) branching ratio

was taken as 0.61 (0.39).[62] The trigger efficiency for γGF charm events with decay muons is 16.7%.

Dimuon events from the decay in flight of muoproduced pions and kaons were simulated with a Monte Carlo program using inelastic structure functions parametrized by the Chicago-Harvard-Illinois-Oxford collaboration.[63] The same experiment provided[64] the π and K production data used to determine final-state particle multiplicities and momentum distributions. Bubble-chamber data[65] were used to parametrize secondary meson-nucleon interactions. This use of experimental input made the Monte Carlo simulation independent of models of hadron production. Hadron trajectories were simulated in the same detail as muon trajectories. The systematic normalization uncertainty in this Monte Carlo simulation was determined to be $\pm 50\%$ by comparing the calculated π, K fraction with that obtained by representing the data as a combination of simulated π-, K-decay, and charm events. The combined trigger and reconstruction efficiency for an event in which a muon scatters and produces a muon from a π or K decay in the shower with an energy greater than 5 GeV is 4.6%.

Cuts are applied to reduce the contribution from π and K decay to $(27 \pm 14)\%$ of the dimuon sample. These cuts require a 9-GeV minimum daughter-muon energy, a minimum ν of 75 GeV, a 0.2-GeV/c minimum daughter-muon momentum, $p_\perp$, traverse to the virtual photon, and a range in inelasticity, $y = 1 - $ (daughter-muon energy)/ν, of $0.675 < y < 0.95$. Histograms of simulated π- and K-decay events are subtracted bin by bin from the data histograms. Almost all of the remaining events are attributed to charmed-meson decay. When these events are simulated with the γGF model, using the Monte Carlo program described above, background-subtracted data and charm Monte Carlo simulation agree adequately in ν, Q^2, y, and daughter-muon energy, while $p_\perp$ is higher in the data by 15%.[58] The measured cross section for diffractive charm production by 209 GeV muons is $6.9^{+1.9}_{-1.4}$ nb.

Monte Carlo simulation of $b\bar{b}$ muoproduction is also based on the γGF model described above. As in the case of charm production, quark pairs carrying the full photon energy are transformed to B mesons using the fragmentation frunction $D(z) = (1-z)^{0.4}$, z is $2\bar{E}_B/m_{b\bar{b}}$, where $\bar{E}_B$ is the B energy in the $b\bar{b}$ reference frame. The B mesons decay to muons via $B \to D\mu\nu$. Further muon-producing cascade decays are ignored, because they tend to

produce decay muons which are indistinguishable from charm background. The diffractive and shadowing parameters used are the same as those used in the ψ Monte Carlo simulation. The simulated detection efficiency for $b\bar{b}$ states decaying directly to at least one muon is 19%.

B. Analysis procedure

The ratio of simulated bottom-quark events to simulated charm-quark events is highest in the region $v > 150$ GeV and $p_\perp > 1.4$ GeV/c. Hereafter we refer to this region as $\mathscr{R}_{b\bar{b}}$. That $\mathscr{R}_{b\bar{b}}$ should contain a higher ratio of $b\bar{b}$ to $c\bar{c}$ may be understood from a model-independent viewpoint in that it takes a higher v to create a heavier quark and a heavier quark produces more $p_\perp$ when it decays. The intent of the $b\bar{b}$ analysis reported here is to reshape slightly the $c\bar{c}$ Monte Carlo distributions in Q^2, y, $p_\perp$, and v in order to achieve full agreement with the data outside $\mathscr{R}_{b\bar{b}}$. This procedure accounts for any inadequacies in modeling the data and reduces the dependence of this analysis on any particular model of heavy-quark production. The reshaping is verified by requiring agreement between data and Monte Carlo simulation in all kinematic spectra after all reshaping is completed. The empirically determined event-weighting functions which accomplish this reshaping are extrapolated into $\mathscr{R}_{b\bar{b}}$, and are used to reshape the $c\bar{c}$ Monte Carlo distributions within that region. Since 58% of the events in $\mathscr{R}_{b\bar{b}}$ have $v < 170$ GeV and 50% have $p_\perp < 1.6$ GeV/c, the extrapolation is small for the majority of the events because the extrapolation covers a range which is only 27% of

the kinematic range of the data on which it is based in v and 17% of the range on which it is based in $p_\perp$. Furthermore, the extrapolation is done simultaneously in two dimensions in the $p_\perp$-v plane, based on statistics 61 times those in $\mathscr{R}_{b\bar{b}}$. The errors in the extrapolation are fully propagated and are included in all calculations. The spectra inside $\mathscr{R}_{b\bar{b}}$ of the weighted charm Monte Carlo events and the background-subtracted data are compared to search for a possible $b\bar{b}$ signal.

The charm Monte Carlo spectra were reshaped by weighting each simulated $c\bar{c}$ event by a product of three functions, respectively of Q^2, y, and (v and $p_\perp$). The weighting functions were $[1 + Q^2/70$ GeV/$c)^2]^{-2}$, a polynomial[66] in y and the function of v and $p_\perp$ listed in Table I. The last function was determined by a two-dimensional fit in the v-$p_\perp$ plane. Since Q^2 and y are only weakly correlated with $p_\perp$ and v it was possible to determine the three weighting functions by iteration. After weighting by all three functions, each event was added to each histogram to produce the reshaped spectra. Before and after weighting, the charm Monte Carlo sample was normalized to the background-subtracted data outside $\mathscr{R}_{b\bar{b}}$.

C. Results

Figures 13 and 14 show background-subtracted data compared to the original and weighted $c\bar{c}$ Monte Carlo spectra in Q^2 and y. Also shown is $100 \times$ the $b\bar{b}$ signal (with $\sigma B = 0.16 \times 10^{-36}$ cm^2) expected from the γGF model. These spectra are populated only by events outside of $\mathscr{R}_{b\bar{b}}$. Figures 15 and 16 make the same data-$c\bar{c}$-$b\bar{b}$ comparison.

TABLE I. Weighting function $R(v, p_\perp)$ for daughter-muon momentum transverse to the virtual photon, $p_\perp$, and beam-muon energy loss v.

$f = \log_{10}(p_\perp)$

$R(v,f) = P(v,f)F(f)$

$P(v,f) = 1.43 + a_0 v + b_0 f + c_0 v \cdot f + d_0 v^2 + e_0 f^2$

$F(f) = (L_1(f) + L_2(f))/(L_3(f) + L_4(f))$

$L_i(f) = (a_i + b_i f)/(|c_i - f|^{d_i} + e_i)(1 \leq i \leq 4)$

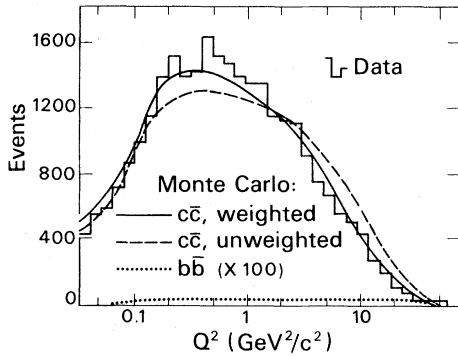| i	a_i	b_i	c_i	d_i	e_i
0	-0.0022	-0.086	-0.0021	-9.3×10^{-6}	-0.57
1	181	165	-0.17	2.1	0.04
2	-0.032	0.031	0.29	5.7	2.8×10^{-5}
3	44	3.9	-0.20	2.6	0.010
4	-0.0045	0.0074	0.30	6.4	9.8×10^{-6}

FIG. 13. Original and weighted $c\bar{c}$ Monte Carlo Q^2 spectra, compared with data after subtraction of the simulated π- and K-decay background. All events lie outside of $\mathscr{R}_{b\bar{b}}$, the region where $\nu > 150$ GeV and the momentum $p_\perp$, of the daughter muon transverse to the virtual photon exceeds 1.4 GeV/c. Also shown is the simulated Q^2 spectrum for $100\times$ the $b\bar{b}$ signal expected from the γGF model.

Figure 15 displays the ν spectra for $p_\perp > 1.4$ GeV/c and $p_\perp < 1.4$ GeV/c, and Fig. 16 shows the $p_\perp$ spectra for $\nu > 150$ GeV and $\nu < 150$ GeV. These figures emphasize the consistency between data and reshaped charm Monte Carlo distributions outside $\mathscr{R}_{b\bar{b}}$. Specifically, in the ν-$p_\perp$ plane outside $\mathscr{R}_{b\bar{b}}$ the χ^2 for a unit ratio of data to the $c\bar{c}$ Monte Carlo simulation is 190 for 176 degrees of freedom.

The region $\mathscr{R}_{b\bar{b}}$ contains 3.4 simulated $b\bar{b}$ events, or 29.5% of the Monte Carlo $b\bar{b}$ sample, and 455
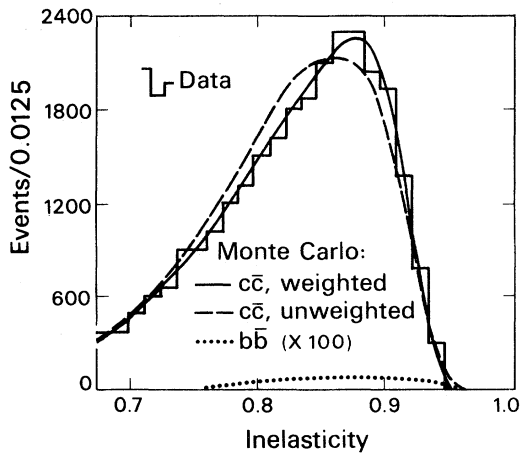
FIG. 14. Original and weighted $c\bar{c}$ Monte Carlo inelasticity $y = 1 - $(daughter-muon energy)/$\nu$, compared with background subtracted data, for events lying outside of $\mathscr{R}_{b\bar{b}}$. Also shown is the simulated y spectrum for $100\times$(the bb signal expected from the γGF model).
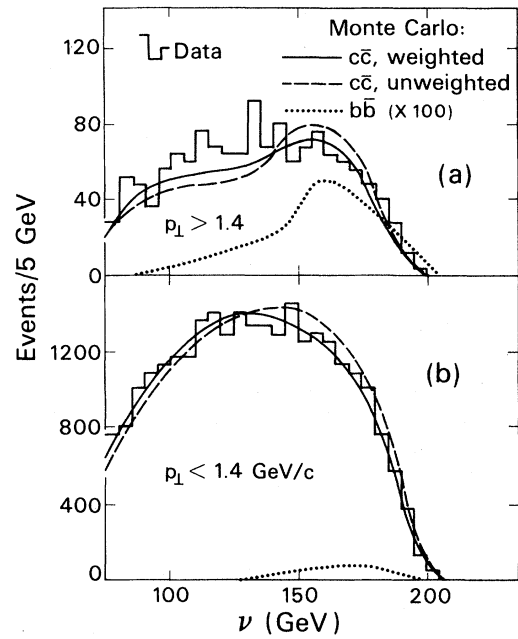
FIG. 15. Original and weighted $c\bar{c}$ Monte Carlo spectra, compared with background-subtracted data for (a) $p_\perp > 1.4$ GeV/c and (b) $p_\perp < 1.4$ GeV/c. Also shown are the simulated ν spectra for $100\times$(the $b\bar{b}$ signal expected from the γGF model).
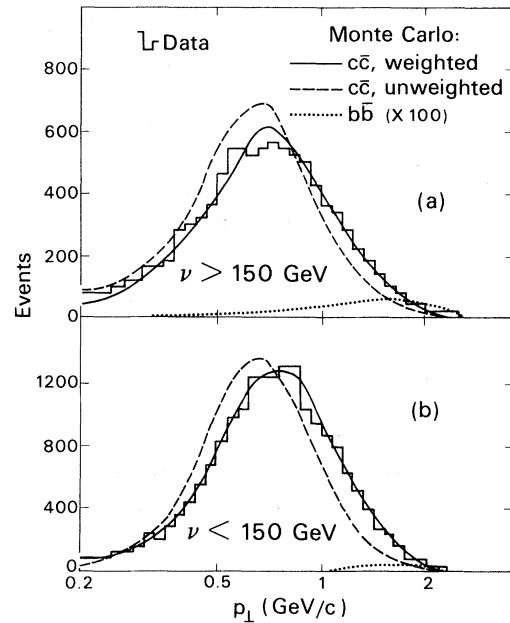

FIG. 16. Original and weighted $c\bar{c}$ Monte Carlo $p_\perp$ spectra, compared with spectra of background subtracted data for (a) $\nu > 150$ GeV and (b) $\nu < 150$ GeV. Also shown are the simulated $p_\perp$ spectra for $100\times$(the $b\bar{b}$ signal expected from the γGF model).

$c\bar{c}$ events, or only 1.5% of the weighted Monte Carlo $c\bar{c}$ sample. After subtraction of the four simulated π- and K-decay background events, 456 data events remain in $\mathscr{R}_{b\bar{b}}$. The error in the difference between data and Monte Carlo simulation is $(\sigma_1^2+\sigma_2^2+\sigma_3^2)^{1/2}$, where $\sigma_1=22$ is the random error in the number of background-subtracted data events in $\mathscr{R}_{b\bar{b}}$ and $\sigma_2=37$ is the error in the number of $c\bar{c}$ Monte Carlo events in $\mathscr{R}_{b\bar{b}}$. Included in σ_2 are the random error in the ratio of Monte Carlo simulation to data outside $\mathscr{R}_{b\bar{b}}$, the error in weighting $c\bar{c}$ Monte Carlo events within $\mathscr{R}_{b\bar{b}}$ based on the spectra outside $\mathscr{R}_{b\bar{b}}$, and the random error in the generated number of these events. The error analyses which determine σ_1 and σ_2 take fully into account the statistical effects of variations in the amount of subtracted background and in the weights assigned to individual events. The systematic error induced by uncertainty in π- and K-decay background, $\sigma_3=20$, is determined by repeating the entire analysis with the background multiplied by 0.5 or 1.5. The resulting $b\bar{b}$ signal in the data is (1 ± 48) events, corresponding to fewer than 62 candidates with 90% confidence. To ensure that any $b\bar{b}$ events outside $\mathscr{R}_{b\bar{b}}$ do not affect the number of expected $c\bar{c}$ events in $\mathscr{R}_{b\bar{b}}$, the analysis was repeated with $14\times$[the simulated $b\bar{b}$ signal (corresponding to 48 events in $\mathscr{R}_{b\bar{b}}$)] added to the background-subtracted data. The simulated $c\bar{c}$ signal in $\mathscr{R}_{b\bar{b}}$ changed by less than one event.

With our luminosity and calculated detection efficiency, these <62 candidates produce the 90%-confidence limit $\sigma(\mu N\rightarrow b\bar{b}X)B(b\bar{b}\rightarrow\mu X)$ $<2.9\times10^{-36}$ cm^2. After factoring out the equivalent flux[67] of transversely polarized virtual photons, the muoproduction limit restricts $\sigma(\gamma N\rightarrow b\bar{b}X)<4.3$ nb at an average virtual photon energy of 160 GeV, when the same branching ratio assumption is made.

Our limits are greater than some published predictions using γGF calculations, but conflict with others and with several vector-meson-dominance (VMD) models. The γGF calculations in Refs. 68 and 69 predicted $\sigma(\mu N\rightarrow b\bar{b}X)=1-3\times10^{-36}$ cm^2 and 4×10^{-36} cm^2, respectively. Reference 70 used a γGF model to derive $\sigma(\gamma N\rightarrow b\bar{b}X)=16$ nb at 160 GeV. The authors of Ref. 71 employed a γGF approach with a fixed strong coupling constant to get $\sigma(\gamma N\rightarrow b\bar{b}X)=0.2$ nb. They also obtained $0.02-0.05$ nb with calculations using a running coupling constant with various gluon momentum distributions, but found 22 nb using VMD-based

calculations. The VMD-model calculation of Ref. 72 yielded $\sigma(\gamma N\rightarrow b\bar{b}X)=25$ nb; Ref. 73 predicted $\mathscr{O}(1-10$ nb) on the basis of empirical formulas and a sum rule derived by Shifman et al.[74] The generalized VMD calculation in Ref. 75 found that the $b\bar{b}$ photoproduction cross section could be as high as 125 nb.

VII. RARE MULTIMUON FINAL STATES

The large target and uniform acceptance of this experiment render it ideally suited for a search for small cross-section processes that yield unusual numbers or topologies of muons in the final state. Two complete scans of events selected from the experimental sample produced by 1.4×10^{11} positive and 2.9×10^{10} negative 209-GeV muons have revealed 16 four-muon events and 12 five-muon events. The integrated luminosity of 0.78 $\times10^{39}$ cm^{-2} also produced 31 events of the type $\mu^{\pm}N\rightarrow\mu^{\pm}\mu^{\mp}\mu^{\mp}X$ and 13 events of the type $\mu^{\pm}N\rightarrow\mu^{\pm}\mu^{\pm}\mu^{\pm}X$. We refer to these two types as odd-signed trimuons to distinguish them from common trimuon production: $\mu^{\pm}N\rightarrow\mu^{\pm}\mu^{\pm}\mu^{\mp}X$. In every event all outgoing muons are fully momentum analyzed and their momenta are checked for energy conservation by including measurement of the incident muon momentum and calorimetric measurement of the associated shower energy. No reports of muon-induced odd-signed trimuons or four- or five-muon final states have been published. Therefore we define these types of events as "rare" events.

A. Analysis

This sample of rare multimuon final states was culled from an initial sample of events in which the preliminary track reconstruction found sufficient candidate tracks which could be attached to the event vertex and provide the appropriate final-state configuration of a rare event. Computer-drawn pictures of these events were scanned by physicists and the legitimate events were selected, for which ~1 m^2 pictures were generated containing all raw wire-chamber hits resolved to better than 1 mm in real transverse coordinates. With the high-resolution pictures, raw chamber hits were reconstructed by hand into tracks and the vertex position was determined. The track reconstruction was then forced to fit the event using the hand-

selected information. The information from the computer reconstruction as to the X^2 of each track and the probability that each chosen wire hit belongs on the track was examined and, if necessary, tracks were altered until the optimum event reconstruction was obtained.

To be accepted as a rare event, the result of the computer-assisted hand-forced fit is required to display the same topology as that of the original reconstruction. Close inspection of each high-resolution picture insures that additional tracks crossing as few as three chambers have not been missed and that distinct tracks separated along their length by as little as 5 mm have not been combined. Figures 17, 18, and 19 show representa-

tive pictures of an odd-signed trimuon, a four-muon event and a five-muon event, respectively.

Several precautions assure that events are legitimate and ensure that two interactions are not mistakenly superimposed: the trigger demands only one beam track within a 57-nsec window centered on the event. All tracks are required to emanate from a tightly defined common vertex. All tracks are required to intersect the appropriate fine-grained hodoscope scintillators, sensitive within a ± 10 nsec window. Adjacent drift and proportional chamber hits are required to register at a level rejecting tracks out of time by more than ~ 50 nsec. The accepted tracks satisfy a tight X^2 cut separately in both orthogonal views. At least three hits in the third view link the two projections. Each accepted track, passing smoothly through > 12 absorption lengths of steel can be interpreted only as a muon. The sign of each muon's charge is at least 8 standard deviations from the reversed value,
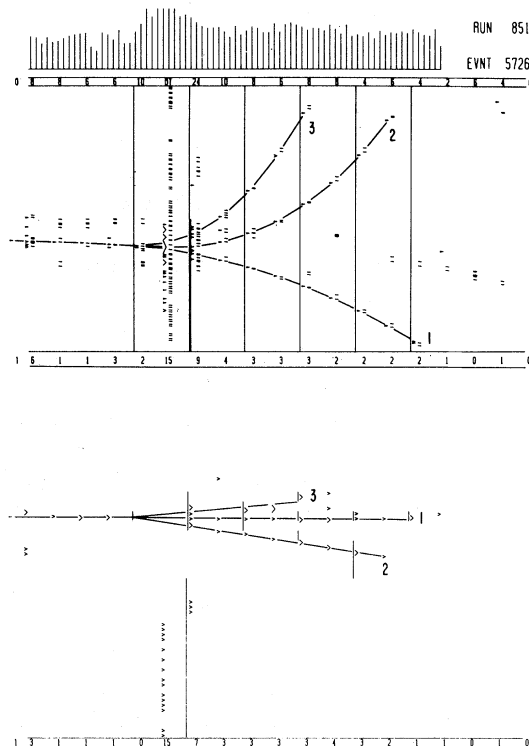

FIG. 17. Computer-generated picture of odd-sign trimuon event 851-5726. Top frame: plan view; bottom frame: elevation view. Superimposed digits are the track numbers mentioned in Table II. Typically, in each interstice between modules a track registers in a proportional chamber (left tic) and, in the plan view, also in a drift chamber (right tic closest to left tic). The drift chambers are noisier due to their longer live time. Short vertical lines at the top are calorimeter counter pulse heights. The vertical lines in the two frames are projections of trigger counters which were tagged. Heavy broken lines are tracings of the computer-reconstructed trajectories.

FIG. 18. Computer generated picture of four-muon event 1191-5809. Top frame: plan view; bottom frame: elevation view. Superimposed digits are the track numbers mentioned in Table IV. Typically, in each interstice between modules a track registers in a proportional chamber (left tic) and, in the plan view, also in a drift chamber (right tic closest to left tic). Short vertical lines at the top are calorimeter counter pulse heights. The vertical lines in the two frames are projections of trigger counters which were tagged. Heavy broken lines are tracings of the computer-reconstructed trajectories.
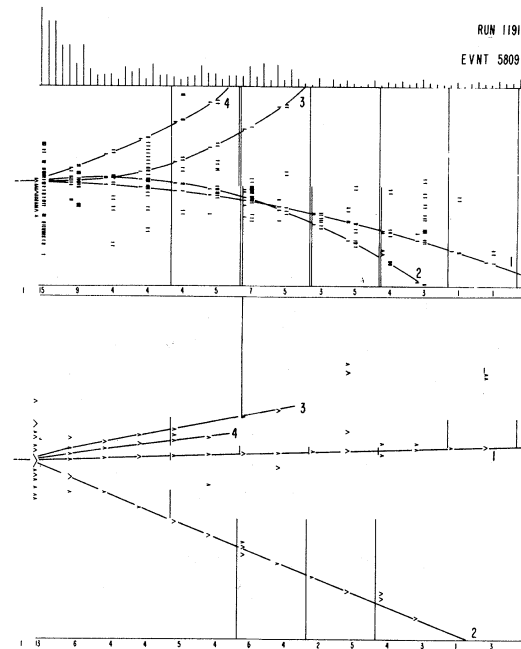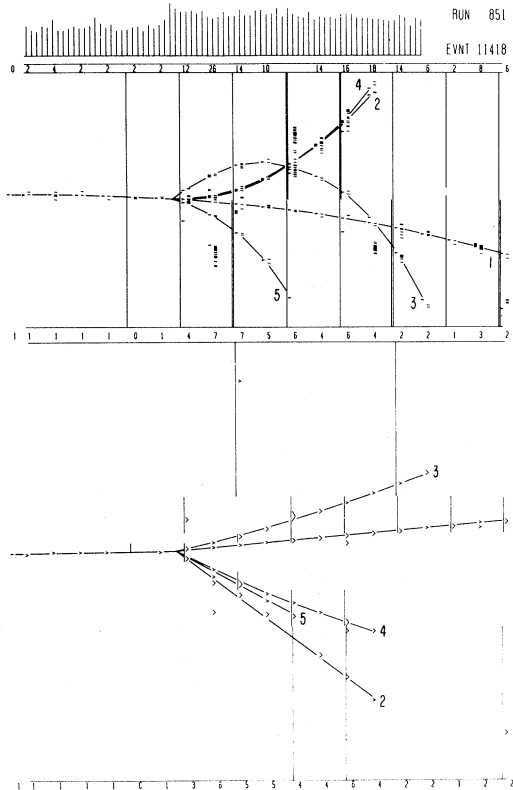
FIG. 19. Computer generated picture of five-muon event 851-11418. Top frame: plane view; bottom frame: elevation view. Superimposed digits are the track numbers mentioned in Table VI. Typically, in each interstice between modules a track registers in a proportional chamber (left tic) and, in the plan view, a drift chamber (right tic closest to left tic). Tracks 3 and 4, while close in the plan view, are connected by diagonal plane-wire hits to clearly separated tracks in the elevation view. Short vertical lines at the top are calorimeter counter pulse heights. The vertical lines in the two frames are projections of trigger counters which were tagged. Heavy broken lines are tracings of the computer reconstructed trajectories.

as determined by the error in its fit curvature.

Tables II–VII present the properties of the rare multimuon events found by two complete scans of the data sample. These scans reveal scanning efficiencies of $\sim 90\%$ for all three types of rare events. Of the original sample of events found by the scan and passing reconstruction, the following pass the tight cuts: 7 of the type $\mu^+ N$ $\rightarrow \mu^+ \mu^+ \mu^+ X$, 22 of $\mu^+ N \rightarrow \mu^+ \mu^- \mu^- X$, 1 of $\mu^- N \rightarrow \mu^- \mu^- \mu^- X$, 6 of $\mu^- N \rightarrow \mu^- \mu^+ \mu^+ X$, 6 of $\mu^+ N \rightarrow \mu^+ \mu^+ \mu^- \mu^- X$, 8 of $\mu^+ N \rightarrow \mu^+ \mu^+ \mu^+ \mu^- X$, 1 of $\mu^- N \rightarrow \mu^- \mu^- \mu^+ \mu^+ X$, 5 of $\mu^+ N$ $\rightarrow \mu^+ \mu^+ \mu^+ \mu^- \mu^- X$, and 5 of $\mu^- N$

$\rightarrow \mu^- \mu^- \mu^- \mu^+ \mu^+ X$. These events are produced in a data sample that contains 75 906 $\mu^\pm N \rightarrow \mu^\pm \mu^\pm X$, 112 369 $\mu^\pm N \rightarrow \mu^\pm \mu^\mp X$, and 110 626 $\mu^\pm N \rightarrow \mu^\pm \mu^\pm \mu^\mp X$. All of the events mentioned pass the same analysis cuts and all samples contain contributions from the two-muon and three-muon triggers.

B. Odd-signed trimuons

An intriguing possible cause for the odd-signed trimuons is a bottom-hadron cascade, such as $\mu^+ N \rightarrow \mu^+ b \bar{b}$; $\bar{b} \rightarrow \bar{c} \mu^+ \bar{\nu}_\mu$, $\bar{c} \rightarrow$ hadrons; $b \rightarrow c$ + hadrons, $c \rightarrow \mu^+ \bar{\nu}_\mu$ + hadrons. However, the limit on the muoproduction of bottom hadrons set previously, when the muonic branching ratios and reconstruction efficiency are included, implies a maximum of three events from this source. The most probable cause of the odd-signed trimuon events is a dimuon produced by a charmed-particle decay in which an extra muon from a π or K decay was produced in the hadronic shower. If the muon is of the correct sign, it will yield the final-state muon charge configuration of an odd-sign trimuon. The charm dimuon signal is isolated from the data by subtracting off the absolutely normalized amount of π- and K-decay events from the entire dimuon sample.[76] The remaining 100 446 dimuons, which pass the same analysis cuts as 36 of the odd-signed trimuons, are ascribed to charmed-particle decay. Besides the track χ^2 requirement these cuts also demand a shower energy greater than 12.5 GeV and an energy transfer ν greater than 30 GeV.

Odd-signed trimuons may be produced by muoproduction in the shower accompanying a charm dimuon. One source of these extra muons is decay of fragments from the struck nucleon. A strong upper limit on this process can be derived by convolution of the shower energy spectrum of the charm dimuons with the Monte Carlo generated probability to obtain a muon from π or K decay versus shower energy,[77] yielding 70 events, of which $\frac{1}{2}$, or 35 are expected to have the muon of the appropriate charge. Results presented earlier[77] suggest little energy is actually transferred to the target nucleon in charm production. Hence the expected number of these events is much less. Another source of extra muons is the decay of kaons produced by D decay. In 2% of the charm events, a muon is expected from the decay of these kaons. These muons are less energetic than those from prompt D decays and therefore have a small-

TABLE II. Odd-sign trimuons listed by event number followed by the charge of the first through third outgoing muon and their momenta (in GeV/c). Events are produced by an incident μ^+ beam except where noted.

Event	Sign	p_{1X}	p_{1Y}	p_{1Z}	p_{2X}	p_{2Y}	p_{2Z}	p_{3X}	p_{3Y}	p_{3Z}
533- 4135	+++	−1.8	0.6	41.1	−0.2	−0.1	29.5	0.8	−0.5	27.8
544- 284	+++	1.3	0.3	111.0	−0.5	−0.7	7.5	−0.4	0.3	6.7
555-11180	+−−	1.6	0.2	143.6	−1.0	−0.3	12.5	1.3	0.2	8.9
588- 959	+−−	−0.4	−0.3	102.4	−1.2	−0.8	20.7	0.2	−0.1	9.7
588- 1916	+−−	−0.3	−0.2	37.3	−1.2	−0.4	10.1	−0.8	0.4	8.0
611- 3961	+−−	−0.0	−0.0	23.5	0.9	−0.1	17.5	−0.4	0.2	14.3
643- 2708	+−−	−1.3	0.1	79.9	−0.3	−0.7	19.7	0.3	0.3	8.7
644- 8059	+−−	−0.4	−0.1	41.8	−0.4	0.7	23.0	−0.6	0.3	9.8
652- 6550	+−−	−0.3	0.5	28.8	−1.0	−0.1	20.8	−0.2	0.2	9.3
666- 8769	+−−	0.9	1.9	63.9	0.4	0.1	18.3	0.1	0.0	8.2
740- 2613	+−−	0.9	0.2	86.5	0.0	0.1	20.0	−0.1	−0.2	11.5
770-10018	+−−	1.3	1.5	78.2	1.0	−0.1	45.2	0.9	−1.2	11.0
773- 7250	+−−	−1.5	1.4	53.4	0.4	−0.4	24.8	−0.3	−0.3	9.1
808- 5590	+++	−0.3	−0.2	41.2	0.1	−0.8	25.4	−0.6	−0.4	8.8
830- 657	+−−	−0.4	0.0	45.2	−0.4	−0.3	16.6	−0.1	0.3	9.4
847- 2596	−++[a]	0.3	−1.3	44.9	−1.0	0.3	30.9	0.0	0.4	23.2
847- 6635	−++[a]	−0.3	−0.5	86.4	−0.3	0.7	18.9	0.5	−0.1	10.4
851- 5726	−++[a]	−0.6	−0.1	48.9	−0.3	−0.4	18.6	−0.0	0.1	10.7
852- 9466	−−−[a]	−0.0	0.4	32.2	−0.8	−0.6	23.6	−0.0	−0.4	10.0
864- 3605	−++[a]	0.7	−0.0	98.5	−0.3	−0.2	12.0	0.1	−0.2	10.8
873- 7911	−++[a]	0.4	−0.2	34.5	0.9	−0.9	8.7	1.3	−0.0	8.1
885- 3661	−++[a]	−0.0	−0.4	45.8	0.6	−0.0	18.7	−0.2	0.6	12.4
928- 5026	+−−	0.3	−0.1	101.2	0.0	−0.2	20.3	−0.6	−1.3	16.7
932-10333	+++	−0.3	−0.0	59.8	−0.2	0.0	20.9	−0.1	0.1	13.5
975- 7110	+−−	−1.8	0.3	49.3	0.0	1.2	63.6	−0.0	−0.4	12.7
981- 1241	+++	−1.4	0.6	132.4	0.5	−0.4	15.5	0.3	−0.1	7.0
1001- 4560	+−−	−2.1	−0.8	99.7	−0.2	0.8	11.2	−0.0	0.1	9.5
1010- 530	+++	0.6	−0.1	39.0	−0.1	−0.1	7.8	−0.3	−1.0	7.7
1013- 7037	+−−	0.5	0.4	27.7	1.4	−0.3	45.3	0.4	−0.1	14.0
1028- 8809	+−−	−1.0	0.0	85.6	0.3	−0.4	17.1	−0.8	−0.4	9.8
1035- 8075	+++	−0.6	0.1	102.8	0.0	−0.4	11.8	−0.0	−0.4	11.5
1057- 7403	+−−	1.3	0.3	175.7	0.4	−0.7	9.3	−0.3	0.2	7.2
1118- 9435	+−−	−0.8	0.8	98.6	0.0	−0.1	17.0	−0.5	−0.4	16.0
1132- 4519	+−−	−0.3	0.3	67.7	−0.5	−0.2	8.6	−0.3	−0.2	7.3
1202- 9314	+−−	−0.0	0.4	77.5	0.9	−0.3	14.0	0.3	0.1	10.5
1213- 940	+−−	0.9	0.4	145.0	0.2	0.0	12.3	0.5	−0.3	8.0

[a] μ^- beam.

er acceptance. One can observe directly the number of muons produced in showers of single-muon inelastic scattering events. In a sample of 222 158 inelastic muon scattering events there are 133 events having a second muon with a momentum $\gtrsim 5$ GeV/c^2 and an opposite sign from that of the scattered muon, where this second muon can be attached to the event vertex, and the event then passes analysis cuts including a cut requiring the total outgoing energy not to exceed the incoming muon energy by more than 52 GeV. In all these events the second muon did not contribute to the event trigger.

Of the 133 events, a certain number may be due to charmed-particle decay. The measured charm muoproduction cross section at 209 GeV times the branching ratio to muons is $1.29^{+0.36}_{-0.29}$ nb. Of the muons produced by charm, 64% exceed 5 GeV in energy. Therefore, the cross section to produce a muon with an energy greater than 5 GeV from a charm decay is 0.66−1.06 nb. The cross section to scatter and produce a muon from π or K decay with energy greater than 5 GeV is 2.28 nb. The muon from π or K decay has a 79% probability of

TABLE III. Odd-sign trimuons listed by event number followed by the shower energy E_{shwr} deposited in the calorimeter, energy transfer v, momentum transfer squared Q^2, inelasticity y, the momentum $p_\perp$ of the daughter muons perpendicular to the virtual-photon direction, and the missing energy E_{miss}.

Event	E_{shwr} (GeV)	v (GeV)	Q^2 [(GeV/c)^2]	y	$p_\perp$ (GeV/c)	E_{miss} (GeV)
533- 4135	112.0	174.0	18.49	0.67	0.16	−3.2
544- 284	33.7	79.3	0.11	0.82	1.06	31.2
555-11180	35.6	58.7	0.47	0.63	0.19	1.5
588- 959	81.9	113.0	0.23	0.73	1.37	0.6
588- 1916	154.2	176.6	0.19	0.90	1.80	4.1
611- 3916	123.8	180.0	1.41	0.82	0.11	24.4
643- 2708	93.0	132.4	0.74	0.79	0.42	10.9
644- 8059	90.3	170.7	0.07	0.81	1.25	47.6
652- 6550	138.1	183.6	1.55	0.84	1.04	15.4
666- 8769	75.6	138.8	11.69	0.81	0.51	36.6
740- 2613	58.8	122.4	0.01	0.74	0.47	32.0
770-10018	69.4	128.7	5.81	0.56	1.60	3.1
773- 7250	123.5	151.7	8.91	0.78	0.71	−5.6
808- 5590	72.7	208.1	0.33	0.84	1.30	101.2
830- 657	146.0	107.0	0.09	0.84	0.20	−11.1
847- 2956	74.3	166.4	9.44	0.68	0.63	38.1
847- 6635	73.9	124.2	0.73	0.76	0.72	21.0
851- 5726	109.7	156.1	0.16	0.81	0.33	17.1
852- 9466	119.5	183.6	1.18	0.82	1.13	30.5
864- 3605	73.6	114.2	0.04	0.80	0.50	17.7
873- 7911	123.4	173.7	0.20	0.90	2.23	33.3
885- 3661	88.5	165.5	0.78	0.81	0.78	46.0
928- 5026	51.8	138.9	0.86	0.73	1.60	50.1
932-10333	136.0	151.5	0.04	0.77	0.15	−18.8
975- 7110	37.9	130.6	2.61	0.42	1.43	16.4
981- 1241	37.6	72.3	0.34	0.69	1.19	12.3
1001- 4560	48.1	105.8	3.30	0.80	0.65	37.0
1010- 530	169.3	163.2	0.22	0.91	1.28	−21.3
1013- 7037	97.1	178.2	1.20	0.67	1.03	21.7
1028- 8809	75.3	116.0	0.53	0.78	0.98	14.3
1035- 8075	100.8	112.6	0.10	0.79	0.78	−11.5
1037- 7403	16.4	36.4	0.26	0.55	0.29	3.5
1118- 9435	53.4	109.5	1.79	0.70	0.27	23.0
1132- 4519	168.5	140.5	0.50	0.89	0.65	−43.9
1202- 9314	81.0	134.3	1.08	0.82	0.95	28.8
1213- 940	32.3	50.1	0.27	0.60	0.77	−2.4

being reconstructed, whereas the probability from a charm decay is 88%. This makes the ratio of the production of reconstructed muons with more than 5 GeV in energy from charm to that from π and K decay 0.32−0.52. Therefore, 65−76 % of the opposite-sign second muon sample is due to muons produced by π or K decay in a hadronic shower. These 86−100 events yield the probability to produce a muon of a given charge in a hadronic shower of $(3.9-4.5)\times10^{-4}$. Therefore, we expect the charm dimuon sample to produce 39−45 odd-sign trimuons from hadronic shower muoproduction.

In order to further determine if the source of the odd-signed trimuons is hadronic shower muoproduction in the charm dimuon sample, Fig. 20 compares the kinematic spectra of the charm dimuon sample with those of the odd-signed trimuons. We apply a statistical test to these distributions to determine their mutual consistency. The Kolmo-

TABLE IV. Four-muon events listed by event number followed by the charge of the first through fourth outgoing muon and their momenta (in GeV/c). Events are produced by an incident μ^+ beam except where noted.

Events	Signs	p_{1X}	p_{1Y}	p_{1Z}	p_{2X}	p_{2Y}	p_{2Z}	p_{3X}	p_{3Y}	p_{3Z}	p_{4X}	p_{4Y}	p_{4Z}
538- 1662	+ + − −	−0.5	0.1	20.7	−0.4	−0.0	13.5	−0.5	−0.5	20.4	0.1	−0.0	15.6
547- 7704	+ − + +	0.3	0.0	20.9	−0.0	0.2	19.2	−0.7	0.6	27.4	−0.5	0.1	13.5
550- 9806	+ + − −	0.4	0.3	15.6	0.2	−0.3	6.6	0.4	−0.0	30.3	−0.2	−0.3	16.2
613- 3277	+ − + +	1.2	0.2	76.8	0.4	−0.1	16.5	1.7	0.7	17.0	0.0	0.0	8.9
672- 445	+ − + +	1.2	−0.0	96.3	0.1	−0.0	9.0	0.3	0.6	16.3	0.0	0.4	13.1
738- 4419	+ − + +	1.3	−0.2	100.5	1.3	−0.1	39.6	−0.1	−0.0	30.2	−0.5	0.1	8.9
777- 7592	+ + − −	−1.9	−0.3	142.4	0.1	−0.3	19.0	−0.6	0.3	31.2	−0.5	−0.1	23.1
898- 1342	− − + +[a]	−1.1	0.5	86.9	−0.0	0.2	11.4	0.6	0.4	24.6	0.1	−0.2	9.3
1005- 3384	+ − + +	−2.7	0.3	175.0	−0.0	−0.3	28.7	−0.8	0.2	12.6	0.4	−0.6	9.4
1025- 6845	+ − + +	−2.1	−1.1	141.3	−0.7	0.8	57.5	0.3	0.2	16.1	−0.3	−1.0	11.6
1034- 3903	+ + − −	−1.0	0.1	52.0	−1.1	−0.8	31.9	1.4	0.7	29.7	−0.1	−0.0	9.9
1079- 1845	+ − + +	−0.8	−1.0	58.2	−2.1	0.8	64.5	−0.6	−0.2	43.2	−1.0	0.0	11.7
1138-10327	+ − + +	−0.7	−0.1	176.9	0.0	−0.5	12.0	−0.2	0.5	13.4	0.2	−0.0	13.2
1141- 4818	+ + − −	−0.4	−0.2	71.8	0.4	−0.0	27.9	−0.5	0.9	20.0	−0.4	0.1	10.5
1191- 5809	+ + − −	−0.3	0.6	65.5	0.5	−2.2	25.5	1.9	1.0	28.8	0.0	1.0	17.8

[a]μ^- beam.

gorov-Smirnov test is superior to the usual Pearson's χ^2 test for small samples and does not involve the binning of individual observations.[78] Given n independent observations of a variable X denoted X_i, numbered in order of increasing magnitude, define

$$s_n(X) = \begin{cases} 0; & X < X_1 \\ i/n; & X_i \leq X \leq X_{i+1}, \\ 1; & X \geq X_n \end{cases}$$

then the Kolmogorov-Smirnov test consists of

TABLE V. Four-muon events listed by event number followed by the shower energy E_{shwr} deposited in the calorimeter, the energy transfer v, momentum transfer squared Q^2, the momentum $p_\perp$ of the daughter muons perpendicular to the virtual-photon direction, the missing energy E_{miss}, and the invariant masses formed by muons 2 and 3 and muons 2 and 4.

Event	E_{shwr} (GeV)	v (GeV)	Q^2 [(GeV/c)^2]	$p_\perp$ (GeV/c)	E_{miss} (GeV)	M_{23} (GeV/c^2)	M_{24} (GeV/c^2)
538- 1662	76.9	180.9	0.80	0.52	54.5	0.45	0.56
547- 7704	105.4	198.3	0.67	0.28	32.8	0.37	0.37
550- 9806	59.2	186.6	1.69	0.63	74.2	0.64	0.52
613- 3277	24.7	126.2	0.27	1.42	59.2	1.51	0.34
672- 445	39.1	99.7	0.03	0.95	22.2	0.52	0.48
738- 4419	48.1	110.1	0.96	0.74	−16.6	1.24	1.63
777- 7592	−4.0	62.4	0.26	0.62	−7.0	0.81	0.60
898- 1342	72.0	119.7	0.97	0.66	2.5	0.42	0.48
1005- 3384	3.9	24.9	0.46	0.92	−29.7	1.24	1.22
1025- 6845	6.3	76.3	2.17	1.15	−15.2	0.89	2.64
1034- 3903	77.8	154.9	0.37	1.13	5.5	2.92	0.69
1079- 1845	29.5	162.2	0.35	2.12	−1.9	1.43	1.42
1138-10327	0.3	34.8	0.01	0.13	−4.0	1.03	0.57
1141- 4818	48.2	146.2	0.31	0.84	39.6	1.40	0.97
1191- 5809	48.8	153.9	1.29	2.30	32.8	3.49	3.06

TABLE VI. Five-muon events listed by event number followed by the momenta of the outgoing muons (in GeV/c). Odd-numbered muons have the same charge as the incoming beam muon, while even-numbered muons have the opposite charge. Events are produced by an incident μ^+ beam except where noted.

Event	p_{1X}	p_{1Y}	p_{1Z}	p_{2X}	p_{2Y}	p_{2Z}	p_{3X}	p_{3Y}	p_{3Z}	p_{4X}	p_{4Y}	p_{4Z}	p_{5X}	p_{5Y}	p_{5Z}
551- 6849	0.7	0.2	82.5	0.3	−0.2	16.6	0.1	0.0	25.4	−0.1	−0.1	8.0	0.3	0.0	23.9
623- 3285	−0.6	0.0	102.2	0.0	0.4	33.4	−0.3	−0.0	28.4	−0.0	−0.3	14.1	−0.1	−0.2	5.8
803- 6308	1.7	0.0	150.1	0.4	−0.3	31.1	−0.0	−0.0	6.7	0.6	0.2	24.5	0.1	−0.0	4.5
830- 9811	−2.3	0.4	137.2	−0.1	−0.2	15.5	−0.7	0.1	30.3	−0.1	−0.1	11.9	−0.0	0.3	6.3
851-11418[a]	−1.1	1.7	144.1	0.0	1.6	19.0	1.2	0.4	12.6	−0.1	−1.0	15.9	−0.3	−0.6	9.9
851-11970[a]	−2.4	−0.3	162.3	−0.0	−0.3	10.9	−0.7	0.1	30.1	0.1	0.2	5.2	−0.5	−0.4	11.9
859- 4305[a]	0.8	−0.1	61.8	0.4	0.8	47.4	0.5	0.4	59.7	−0.5	−0.3	36.5	−0.1	0.2	4.6
861- 206[a]	0.4	0.1	85.1	−1.1	1.3	38.4	−0.0	−0.1	24.0	−0.0	−0.0	12.4	0.3	1.1	7.3
890- 1460[a]	−0.0	−0.4	79.5	−0.5	−0.0	21.2	0.1	0.1	31.1	0.9	−0.4	20.1	−0.4	0.2	19.3
1095- 9242	1.6	0.4	106.1	0.1	0.3	25.2	0.7	0.2	25.0	0.2	0.2	22.2	0.1	−0.5	8.4

[a] μ^- beam.

finding the maximum of the absolute value of the difference between the $S_n(X)$ for the two distributions. This maximum is then converted into a confidence level through use of calculated tables.[79]

The Kolmogorov-Smirnov test shows some deviations between the dimuon and odd-sign trimuon samples because the generation of an additional muon in a charm dimuon affects the event topology so that the event will appear slightly altered from a typical charm dimuon event even when reconstructed by an analysis blind to the third muon. We believe this effect is probably most pronounced in assessing the inelasticity and shower energy of events. Table VIII presents the results of

the Kolmogorov-Smirnov test on the two samples. In light of their topological differences they display no clear inconsistency. The comparison of the $p_\perp$ spectra is particularly important in that heavy-quark production would produce a large inconsistency since the average bottom decay produces a $p_\perp$ of 1 GeV/c and the average charm decay 0.4 GeV/c. It also should be noted that the six spectra presented in Fig. 20 do not display independent variables if one assumes the parent process involves virtual photoproduction. However, the six could be less correlated were some other "new physics" involved in their creation.

TABLE VII. Five-muon events listed by event number followed by the shower energy E_{shwr} deposited in the calorimeter, the energy transfer ν, the momentum transfer squared Q^2, the momentum $p_\perp$ of the daughter muons perpendicular to the virtual-photon direction, the missing energy E_{miss}, and the invariant masses formed by the pairings of muons 2 and 4 with muons 3 and 5.

| Event	E_{shwr} (GeV)	ν (GeV)	Q^2 [(GeV/c)^2]	$p_\perp$ (GeV/c)	E_{miss} (GeV)	M_{23} (GeV/c^2)	M_{25} (GeV/c^2)	M_{43} (GeV/c^2)	M_{45} (GeV/c^2)
551- 6849	35.8	118.5	0.22	0.41	8.8	0.41	0.36	0.33	0.41
623- 3285	4.4	102.4	0.64	0.82	16.5	0.58	0.50	0.69	0.29
803- 6308	−0.1	61.0	0.02	0.39	−5.7	0.36	0.44	0.33	0.33
830- 9811	5.0	61.6	0.29	0.62	−7.4	0.59	0.39	0.63	0.51
851-11418	3.7	63.2	3.08	1.92	2.0	2.28	1.93	0.57	0.37
851-11970	9.0	45.5	0.08	0.28	−21.6	0.72	0.79	0.85	0.77
859- 4305	4.4	151.0	0.50	1.15	−4.9	1.26	1.26	0.71	0.84
861- 206	16.5	123.5	0.05	0.41	24.8	1.38	0.23	3.18	1.43
890- 1460	45.7	132.8	0.66	0.71	−4.8	0.67	1.16	0.28	1.40
1095- 9242	7.7	96.8	0.19	0.34	8.2	0.67	0.50	0.99	0.88
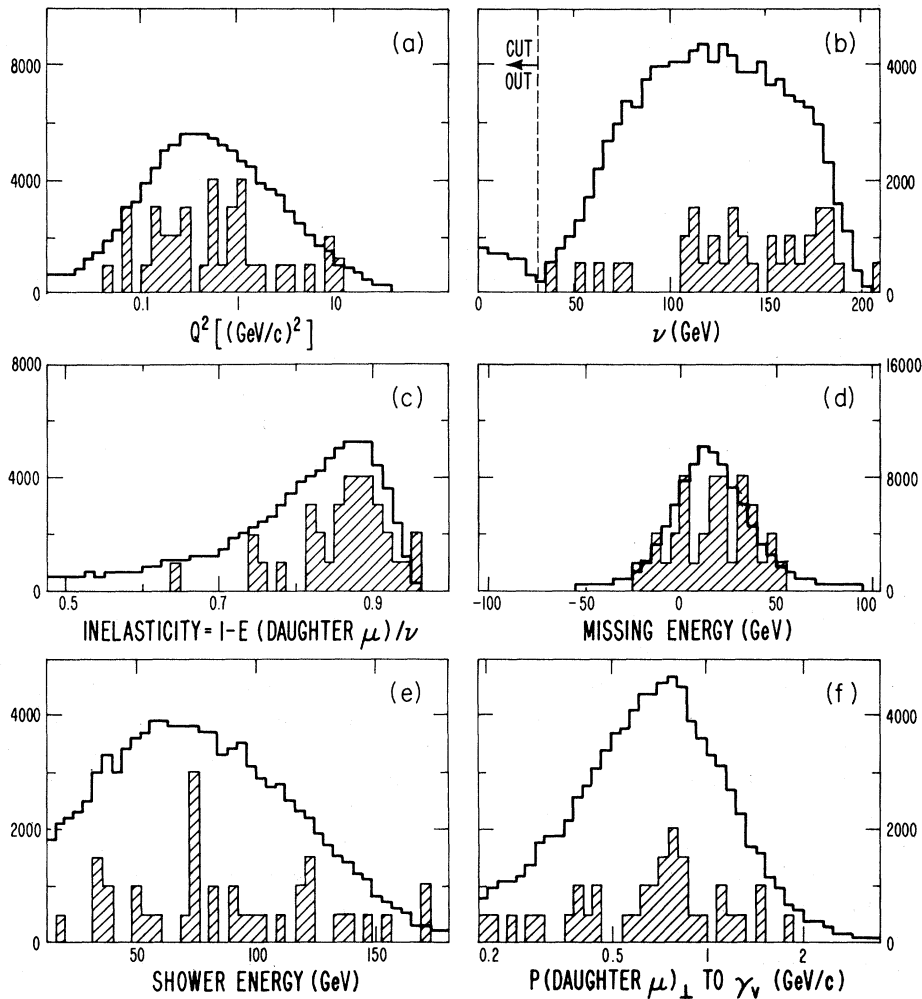
FIG. 20. Distributions in six reconstructed kinematic variables for inelastic dimuons and odd-sign trimuons. Both types of event have shower energy greater than 12.5 GeV and energy transfer v greater than 30 GeV. The inelastic dimuons displayed consist of all dimuons with the properly normalized π- and K-decay Monte Carlo events subtracted off. The vertical scales refer to the dimuons only. The scale for the trimuons is two events per division. The plain histograms represent the dimuons and the slashed columns represent the trimuons. In all distributions except (c), (d), and (e), the trimuons have had their slowest muon removed and are analyzed as dimuons. Distributions shown are (a) momentum transfer squared, (b) energy transfer v, (c) inelasticity, (d) missing energy, (e) shower energy, and (f) the momentum of the daughter muon perpendicular to the virtual-photon direction. All events pass the same standard cuts.

C. Elastic four- and five-muon events

We observe three four-muon events and five five-muon events with a shower energy less than 6 GeV that pass our analysis quality cuts. We define these as elastic events. There are two five-muon events not included in the elastic sample in which the fifth muon track has a poor χ^2 and the remaining four tracks pass the χ^2 cut. The elastic five-muon events are probably due to electromagnetic

tridents in which an extra electromagnetic pair is produced and the four-muon events are five-muon events in which the fifth, presumably low-energy, muon was not seen.

The sources of electromagnetic pairs are shown in Fig. 21 for the case of electromagnetic trident production off a target T. We have done Monte Carlo studies of these processes and conclude that Bethe-Heitler dominates over bremsstrahlung by a factor of 100. Since our experiment does not im-

TABLE VIII. Probability that the inelastic two-muon events have different distributions in the specified kinematic variables from the inelastic odd-sign three-muon events analyzed with N_μ muons. ($N_\mu = 2$ means the lowest-energy track was erased and the event then reanalyzed.)

Variable	N_μ	Probability
Shower energy	3	57%
ν	2 (3)	97% (97%)
Q^2	2 (3)	2% (2%)
$p_\perp$ to γ_V	2 (3)	75% (91%)
Inelasticity	2	99.6%
Missing energy	3	42%

pose an opening angle cut on the outgoing muons, this ratio agrees with that found by Ref. 80 for a coherent iron target without cuts. We therefore believe the dominant contribution to the elastic four- and five-muon events to be the double Bethe-Heitler diagram shown in Fig. 22(a).

In order to study the double Bethe-Heitler process we first consider single Bethe-Heitler events which constitute 99% of our electromagnetic tri-

dent sample. Examination of the elastic (shower energy less than 6 GeV) trimuon sample reveals a large contribution from elastic ψ production. The number of elastic ψ's is determined by fitting the dimuon invariant-mass continuum above and below the region of charmonium production, extrapolating this fit into the region of charmonium production and subtracting the fit number of continuum events from the total in this region. The remaining events are ascribed to ψ and ψ' production. This number of elastic ψ and ψ' Monte Carlo events[81] is then subtracted from the entire elastic trimuon sample, leaving 87 650 events attributed to electromagnetic trident production. All of these events pass the same analysis quality cuts as the four and five-muon events.

The expected number of elastic four- and five-muon events due to electromagnetic tridents generating an additional pair via a double Bethe-Heitler process is estimated two ways. First, and most simply, these events are expected to appear with a frequency of $O(\alpha^2)$ less than electromagnetic tridents. This predicts six events. Second, the probability for a photon with sufficient energy to produce a muon pair, where each muon exceeds the detection threshold energy of ~ 5 GeV, may be
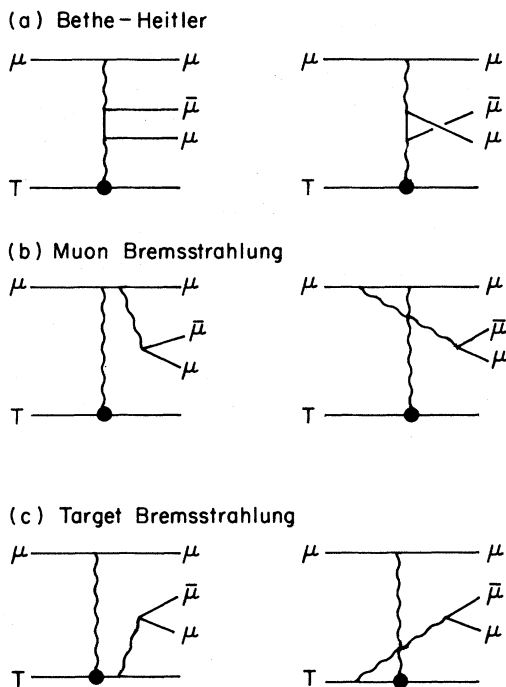

FIG. 21. Feynman diagrams for the electromagnetic production of muon tridents for a target T: (a) Bethe-Heitler, (b) muon bremsstrahlung, (c) target bremsstrahlung. From Ref. 90.
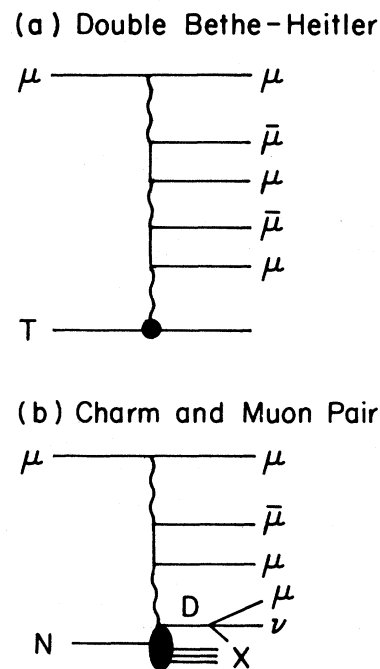

FIG. 22. Feynman diagrams for the electromagnetic production of a muon pair in (a) an electromagnetic trident (Double Bethe-Heitler) off a target T, and in (b) a charm dimuon.

determined by comparing the total electromagnetic trident sample with the virtual photon flux that produced it. Inelastic ψ and ψ' events are subtracted off the inelastic trimuon sample as in the elastic case to determine the inelastic portion of the electromagnetic trident sample. When added to the elastic tridents, they comprise the total 104 496 events in the electromagnetic trident sample.

The equivalent flux[82] of transversely polarized virtual photons per muon is multiplied by the incoming flux of 1.7×10^{11} muons. The data corresponds to 2.04×10^9 virtual photons with $\nu > 10$ GeV. This yields a probability of 5.1×10^{-5} to produce an extra pair, and have it trigger and be reconstructed. In the entire sample of four- and five-muon events $(52 \pm 19)\%$ would not have triggered without the presence of the additional muons beyond the spectator and the most energetic daughter muon of each sign. Therefore, folding in its additional probability for triggering, the expected rate for a virtual photon to produce an additional electromagnetic pair is 1.1×10^{-4}. This then predicts 9.6 elastic electromagnetic four- and five-muon events.

To further test the hypothesis that the elastic four- and five-muon events are due to double Bethe-Heitler production, they may be compared with the events principally due to single Bethe-Heitler production, the elastic electromagnetic tridents. Figure 23 compares the spectra of various kinematic quantities for the elastic four- and five-muon events with the elastic tridents. Table IX presents the probability that these various kinematic spectra are consistent based on the application of the Kolmogorov-Smirnov test. The conclusion is that the elastic electromagnetic tridents form the parent sample of the elastic four- and five-muon events.

D. Inelastic four-muon events

There are 13 four-muon events which have a shower energy greater than 6 GeV. Of these inelastic events there are 11 which have a shower energy greater than 12.5 GeV and a ν greater than 30 GeV. We believe these events are inelastic dimuons, primarily due to charm particle production with muonic decay, accompanied by the electromagnetic production of a muon pair. The diagram for this reaction is shown in Fig. 22(b). After subtraction of the π- and K-decay background there are 100 446 dimuon events passing analysis cuts with a shower energy greater than

12.5 GeV and ν greater than 30 GeV. These are ascribed principally to charmed meson production with a muonic decay. The previously determined probability to electromagnetically produce a muon pair of 1.1×10^{-4} yields 11 four-muon events expected from charm events with an additional electromagnetic pair.

Figure 24 compares the spectra of various kinematic quantities for the four-muon events and the background subtracted dimuon events, where all events have a shower energy exceeding 12.5 GeV and a ν exceeding 30 GeV. Table X presents the probability that these spectra are consistent, based on the application of the Kolmogorov-Smirnov test. The conclusion is that charm dimuons electromagnetically producing a muon pair are the most likely source for these inelastic four-muon events.

Another possible source of the 13 inelastic four-muon events is that of an inelastic trimuon with an additional muon from a π or K decay in the hadronic shower. The inelastic (shower energy greater than 6 GeV) portion of the electromagnetic trident sample includes 16 845 events. The previously determined probability to produce a muon of a given charge in an hadronic shower exceeding 6 GeV of $(3.9 - 4.5) \times 10^{-4}$ predicts $6 - 8$ muons of each sign produced in the hadronic showers of the inelastic tridents. Thus up to $12 - 16$ of the four-muon events could be produced by muoproduction in the hadronic showers of the inelastic tridents. The spectra of various kinematic quantities of the inelastic four-muon events are compared with the spectra for the inelastic tridents in Fig. 25.

Table XI presents the probability that the spectra of the combined inelastic four- and five-muon

TABLE IX. Probability that the elastic three-muon events have different distributions in the specified kinematic variables from the elastic five-muon events analyzed with N_μ muons.

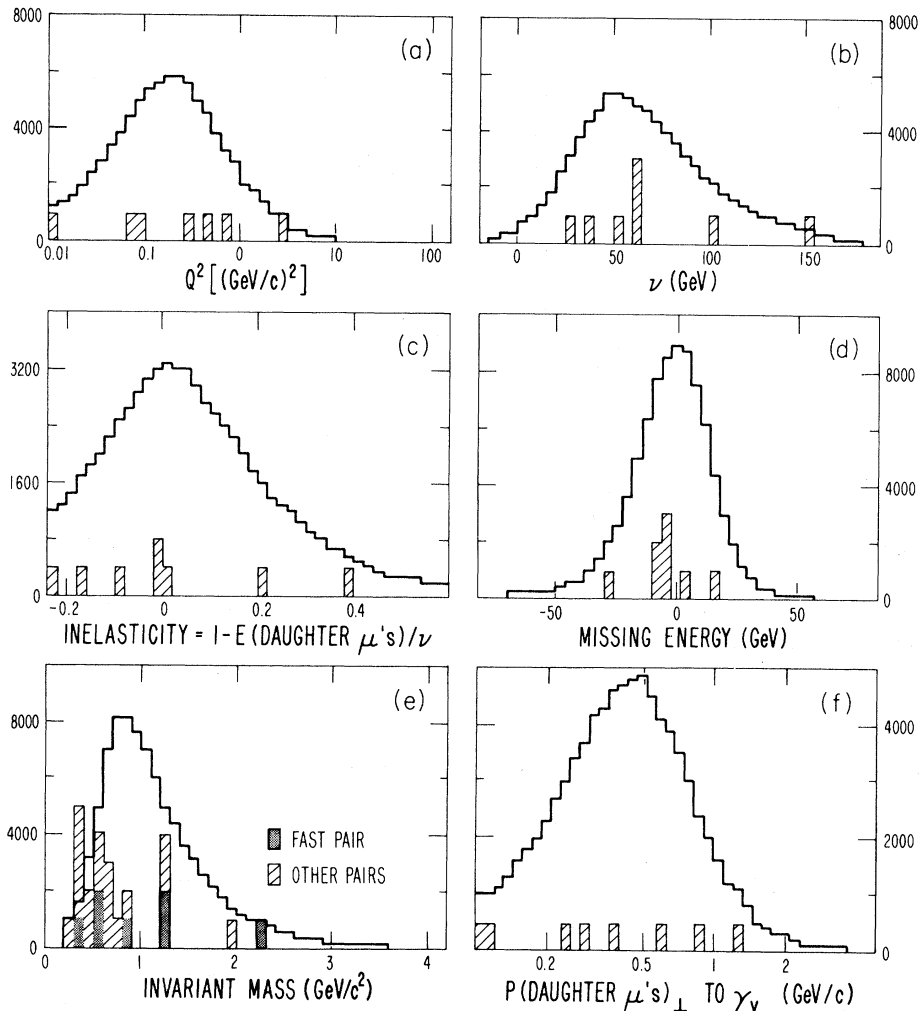| Variable	N_μ	Probability
Shower energy	5	56%
ν	3 (5)	55% (82%)
Q^2	3 (5)	30% (38%)
$p_\perp$ to γ_V	5	$\frac{1}{2}\%$
Inelasticity	3 (5)	58% (30%)
Missing energy	5	63%
Invariant mass	3 (5)	6% (15%)

FIG. 23. Distributions in six reconstructed kinematic variables for elastic tridents and elastic four- and five-muon events. Both types of event have shower energies less than 6 GeV. The elastic tridents consist of all elastic trimuons with the properly normalized ψ Monte Carlo events subtracted off. The vertical scales refer to the tridents only. The scale for four- and five-muon events is two events per division. The plain histograms represent the tridents and the slashed columns represent the four- and five-muon events. In all distributions except (c) and (d), the four- (five-) muon events have had their slower muon(s) removed and are analyzed as tridents. Distributions shown are (a) momentum transfer squared, (b) energy transfer v, (c) inelasticity, (d) missing energy, (e) invariant mass of the daughter-muon pairs, which for the four- and five-muon events includes all possible pairings with the pairing produced by the two most energetic (fast) muons with the appropriate signs being shaded, and (f) the momentum of the daughter muons together perpendicular to the virtual photon direction. All events pass the same standard cuts.

sample are consistent with those of the inelastic tridents, and Table XII presents the probability that the spectra of the inelastic five-muon events are consistent with those of the inelastic tridents. These probabilities, based on the Kolmogorov-Smirnov test, show that while the spectra of the combined sample are not consistent with the inelastic tridents, the inelastic five-muon events by themselves are consistent. Therefore the incon-

sistency between the combined sample and the inelastic tridents is due to the inelastic four-muon events. It is evident that the contribution of inelastic tridents with hadronic shower muoproduction to the inelastic four-muon sample must be small. The primary source of the inelastic four-muon events is charm production with electromagnetic pairs.

One inelastic four-muon event bears further ex-

TABLE X. Probability that the inelastic two-muon events have different distributions in the specified kinematic variables from the inelastic four-muon events analyzed with N_μ muons.

Variable	N_μ	Probability
Shower energy	4	92%
ν	4 (2)	70% (70%)
Q^2	4 (2)	37% (66%)
$p_\perp$ to γ_V	2 (4)	30% (51%)
Inelasticity	2	36%
Missing energy	4	71%

TABLE XII. Probability that the inelastic three-muon events have different distributions in the specified kinematic variables from the inelastic five-muon events when they are analyzed with N_μ muons.

Variable	N_μ	Probability
Shower energy	5	1%
ν	3 (5)	9% (40%)
Q	5 (3)	8% (25%)
p to γ_V	5 (3)	52% (54%)
Inelasticity	5	1%
Missing energy	5	30%
Invariant mass	5	60%

amination. Event 1191-5809 has an unusually high transverse momentum with respect to its virtual photon of 2.3 GeV. The probability that the two conventional processes here considered to be the source of the four-muon events would produce one or more four-muon events with a $p_\perp$ greater than or equal to that of event 1191-5809 is 11%. The invariant masses of the two possible muon pair combinations are 3.5 and 3.0 GeV. The probability of producing an inelastic four-muon event with a reconstructed invariant mass within one standard deviation (9%) of the ψ mass is also 11%. These and other considerations have prompted the interpretation[83] of this event as diffractive $b\bar{b}$ production with $\bar{b} \to \psi X$, $\psi \to \mu^+ \mu^- X$, and $b \to \mu^- \bar{\nu}_\mu X$.

E. Inelastic five-muon events

There are five five-muon events with a shower energy greater than 6 GeV. The most probable source for these events is that of an inelastic trimuon with an additional electromagnetically produced

muon pair. The number of events due to such an inelastic double Bethe-Heitler process may be estimated by using the previously determined probability to electromagnetically produce a muon pair of 1.1×10^{-4}. This probability, when multiplied by the inelastic trident sample of 16 845 events, yields two expected inelastic five-muon events.

Another possible source of muon pairs would be their production in the hadronic shower of the inelastic tridents. However, the cross section for muon-induced hadronic pair production in Ref. 84 is less by a factor of 23 than the cross section for the muon-induced Bethe-Heitler process in Ref. 85. As mentioned earlier, other radiated sources of pairs are suppressed by a factor of 100 with respect to the Bethe-Heitler process. Figure 25 displays the spectra of various kinematic quantities of the inelastic five-muon events with the spectra of the inelastic tridents. Table XII presents the probability that the spectra of the inelastic five-muon events are consistent with those of the inelastic tridents.

TABLE XI. Probability that the inelastic three-muon events have different distributions in the specified kinematic variables from the inelastic four- and five-muon events analyzed with $\leq N_\mu$ muons.

Variable	N_μ	Probability
Shower energy	5	99.5%
ν	5 (3)	99.9% (99.98%)
Q	3 (5)	82% (87%)
p to γ_V	3 (5)	92% (98%)
Inelasticity	5	91%
Missing energy	5	99%
Invariant mass	5 (3)	66% (82%)

TABLE XIII. Numbers of exotic multimuon events categorized by type and shower energy E_{shwr} from data corresponding to an integrated luminosity of 0.78 $\times 10^{39}$ cm^{-2}. Also included are the expected number of events as explained in the text.

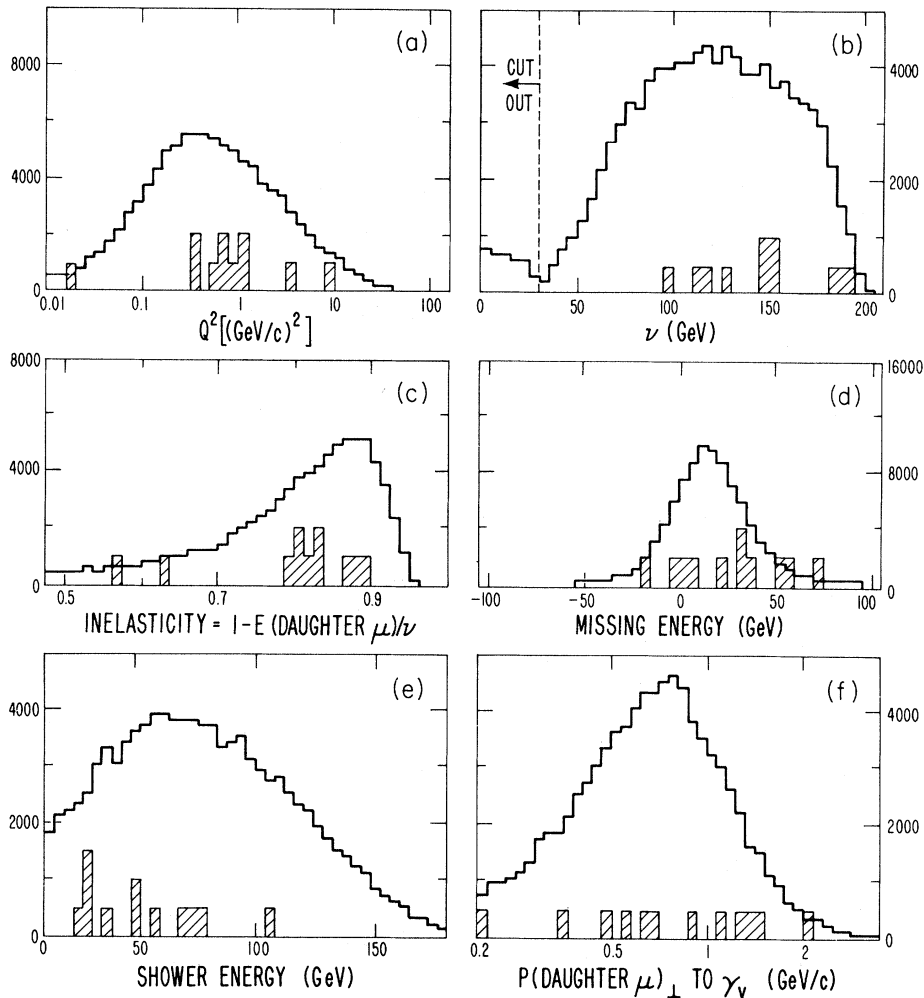| Event	E_{shwr} (GeV)	Number	Expected
$\mu^+ \to \mu^+ \mu^\pm \mu^\pm$	> 12.5	36	39−45
$\mu^+ \to \mu^+ \mu^- \mu^+ \mu^\pm$	< 6	3	< 10
	> 6	13	11−27
$\mu^+ \to \mu^+ \mu^- \mu^+ \mu^- \mu^+$	< 6	5	< 10
	> 6	5	2

FIG. 24. Distributions in six reconstructed kinematic variables for inelastic dimuons and inelastic four-muon events. Both types of events have shower energy greater than 12.5 GeV and energy transfer greater than 30 GeV. The inelastic dimuons displayed consist of all dimuons with the properly normalized π- and K-decay Monte Carlo events subtracted off. The vertical scales refer to the dimuons only. The scale for the four-muon events is two events per division. The plain histograms represent the dimuons and the slashed columns represent the four-muon events. In all distributions except (c), (d), and (e), the four-muon events have had the slower muon of each sign removed and are analyzed as dimuons. Distributions shown are (a) momentum transfer squared, (b) energy transfer v, (c) inelasticity, (d) missing energy, (e) shower energy, and (f) the momentum of the daughter muon perpendicular to the virtual photon direction. All events pass the same standard cuts.

The conclusion is that the inelastic five-muon events appear due to the inelastic double Bethe-Heitler process.

It is interesting to observe the sign of the beam muon producing the five-muon events. The data sample which contains these events was induced by $1.4 \times 10^{11} \mu^{+}$ and $2.9 \times 10^{10} \mu^{-}$, a ratio of μ^{+}/μ^{-} of 5. However, of the five inelastic five-muon events, three were produced by the μ^{-} beam. Overall, for the entire five-muon sample, five are

μ^{+} induced and five are μ^{-} induced. In addition one of the elastic μ^{-}-induced five-muon events, 851-11418, has particularly remarkable characteristics in that it has a Q^{2} of 3 GeV and a total transverse momentum with respect to the virtual photon of 2 GeV. The probability that the double Bethe-Heitler process would produce one or more events with a $p_{\perp}$ and Q^{2} greater than or equal to the values of event 851-11418 is 3%, based on the single Bethe-Heitler kinematic distributions.
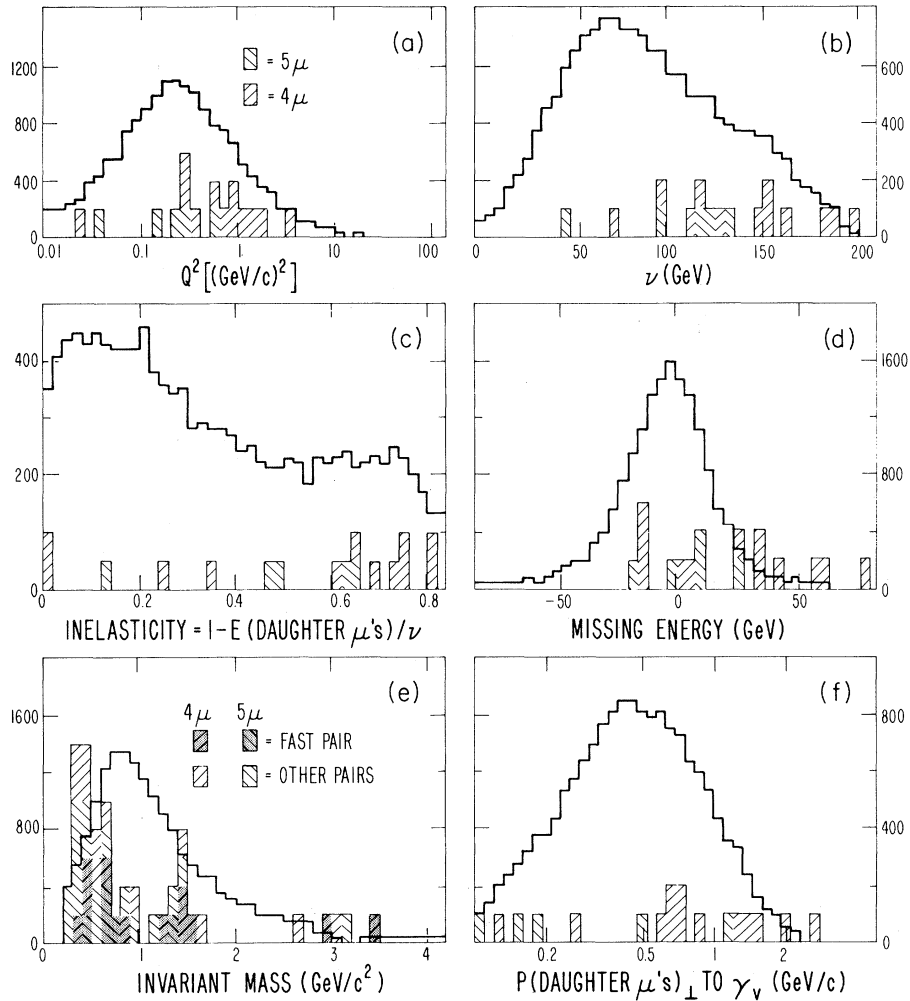
FIG. 25. Distributions in six reconstructed kinematic variables for inelastic tridents and inelastic four- and five-muon events. All events have shower energy greater than 6 GeV. The inelastic tridents displayed consist of all trimuons with the properly normalized inelastic ψ Monte Carlo events subtracted off. The vertical scale refers to the tridents only. The scale for the four- and five-muon events is two events per division. The plain histograms represent the tridents while the left to right ascending slashed columns represent the four-muon events and the left to right descending slashed columns represent the five-muon events. In all distributions except (c) and (d) the four- (five-) muon events have had their slower muon(s) removed and are analyzed as trimuons. Distributions shown are (a) momentum transfer squared, (b) energy transfer ν, (c) inelasticity, (d) missing energy, (e) invariant mass of the daughter-muon pairs, which for the four- and five-muon events include all possible pairings with the pairing produced by the two most energetic (fast) muons with the appropriate signs being shaped, and (f) the momentum of the daughter muons together perpendicular to the virtual-photon direction. All events pass the same standard cuts.

F. Other observations

Although there have been no other observation of muon-induced rare multimuon events, there have been observations of neutrino-induced odd-sign trimuons and four-muon events. The CERN-Dortmund-Heideberg-Saclay (CDHS) group report-

ed[86] observing four $\nu \rightarrow \mu^- \mu^+ \mu^+$ events with a calculated background of six events from π and K decays. They also observe[87] one event of the type $\bar{\nu} \rightarrow \mu^+ \mu^- \mu^-$. These events occur at a rate of 1×10^{-6} relative to charged-current neutrino scattering. The CDHS group has also observed[88] one event of the type $\nu \rightarrow \mu^+ \mu^- \mu^+ \mu^-$. The rate

corresponding to the four-muon event relative to the opposite-sign neutrino-induced dimuon events is $\sim 1.4 \times 10^{-4}$.

The Berkeley-Fermilab-Hawaii-Seattle-Wisconsin groups has observed one event of the type $v \rightarrow \mu^+ e^- e^+ e^-$ in the 15-foot bubble chamber at Fermilab.[89] The rate relative to single-muon production for this event is of order 10^{-7}, the same as that corresponding to the CDHS four-muon event. It is important to remember when comparing the muon- and neutrino-induced rare events that in the former case the model involves the interaction of a virtual photon with a sea charm quark and in the latter the interaction of a virtual W with a valence d or s quark.

The rare multimuon events reported here appear to be produced by conventional physics with the possible exception of one elastic five-muon event and one inelastic four-muon event. Nevertheless, diagrams such as those in Fig. 22 have not been observed before. The actual and expected numbers of events of all types are shown in Table XIII. To summarize, the odd-sign trimuons have a rate relative to the dimuons of 3.6×10^{-4} and are due to charm dimuon events accompanied by an additional π or K decay. The elastic four- and five-muon events are electromagnetic in origin, specifically due to the double Bethe-Heitler process and have a rate relative to the elastic tridents of 9×10^{-5}.

The inelastic four-muon events appear to be charm dimuons with an electromagnetically produced muon pair. There could also be a small contribution from inelastic tridents where a muonic π or K decay ocurred in the hadronic shower. The inelastic four-muon events occur at a rate 1.1×10^{-4} relative to the charm dimuons. The kinematics of the inelastic five-muon events are consistent with those of inelastic tridents that electromagnetically produced an additional muon pair.

However, their rate relative to the inelastic tridents is 3×10^{-4}, a rate that is higher than the four-muon rate relative to the dimuons. This is anomalous because both types of event should display the same rate with respect to their parent process if both are due to electromagnetic pair production in the parent process. The observed rate of the four-muon events with respect to the dimuons is consistent with the calculated one, whereas the rate for the five-muon events with respect to the inelastic tridents is not. This anomaly may suggest new physics when considered with the fact that although the ratio of incident positive to negative muon beam fluxes is 5:1, there is an equal number of five-muon events induced by beam muons of each sign. However, the statistics are far from conclusive.

ACKNOWLEDGMENTS

*Now at Columbia University, New York, NY 10025.
†Now at Enrico Fermi Institute, Chicago, IL 60637.
‡Now at Bell Laboratories, Murray Hill, NJ 07974.
[1]S. L. Glashow, Nucl. Phys. 22, 579 (1961); S. Weinberg, Phys. Rev. Lett. 19, 1264 (1967); G. 't Hooft, Nucl. Phys. B33, 173 (1971).
[2]S. L. Glashow, J. Iliopoulos, and L. Maiani, Phys. Rev. D 2, 1285 (1970).
[3]M. Kobayashi and K. Maskawa, Prog. Theor. Phys. 49, 652 (1973).
[4]S. W. Herb et al., Phys. Rev. Lett. 39, 252 (1977); J. K.

B. Bienlein et al., Phys. Lett. 78B, 360 (1978).
[5]G. Moneti, in Weak Interactions, proceedings of the Summer Institute on Particle Physics, SLAC, 1980, edited by Anne Mosher (SLAC, Stanford, 1981).
[6]D. Cline and D. D. Reeder, in Proceedings of the International Symposium on Lepton and Photon Interactions at High Energies, Hamburg, 1977, edited by F. Gutbrod (DESY, Hamburg, 1977).
[7]M. Holder et al., Phys. Lett. 73B, 105 (1978).
[8]R. J. Loveless et al., Phys. Lett. 78B, 505 (1978).
[9]G. Gollin et al., IEEE Trans. Nucl. Sci. NS-26, 59

(1979).

[10]G. D. Gollin *et al.*, Phys. Rev. D 24, 555 (1981).

[11]S. Weinberg, Phys. Rev. Lett. 19, 1264 (1967).

[12]F. Wilczek and A. Zee, Nucl. Phys. B106, 461 (1976).

[13]T. Cheng and L. Li, Phys. Rev. D 16, 1425 (1977).

[14]D. McKay and H. Muczek, Phys. Rev. D 19, 985 (1979).

[15]E. J. Konipinski and H. Mahmoud, Phys. Rev. 99, 1065 (1953).

[16]M. Abud and A. Bottino, Nuovo Cimento 51A, 473 (1979).

[17]Z. Hioke, Prog. Theor. Phys. 58, 1859 (1977).

[18]J. Kandaswamy and J. Schecter, Phys. Rev. D 15, 251 (1977).

[19]S. Weinberg and B. W. Lee, Phys. Rev. Lett. 38, 1237 (1977); Y. Achiman and B. Stech, Phys. Lett. 77B, 384 (1978). These models and those of Refs. 12−18 often specify μ^+-$\overline{M}^0$ couplings of Fermi strength with $m_{M^0} \approx 4-5$ GeV/c^2 and $B(M^0 \rightarrow \mu^+\mu^-\nu_\mu) \simeq 0.1-0.2$.

[20]K. W. Rothe and A. M. Wolsky, Nucl. Phys. B10, 241 (1969).

[21]A. E. Asratyan, *et al.*, Phys. Lett. 49B, 488 (1974).

[22]T. Eichten *et al.*, Phys. Lett. 46B, 281 (1973).

[23]B. C. Barish *et al.*, Phys. Rev. Lett. 32, 1387 (1974).

[24]D. S. Baranov *et al.*, Phys. Lett. 81B, 261 (1979), Yad. Fiz. 29; 1206 (1979) [Sov. J. Nucl. Phys. 29, 622 (1979)].

[25]D. Rein, L. M. Sehgal, and P. M. Zerwas, Nucl. Phys. B138, 85 (1978); Y. Abe and Y. Hoshino, Prog. Theor. Phys. 60, 513 (1978); G. G. Volkov *et al.*, Yad. Fiz. 27, 1608 (1978) [Sov. J. Nucl. Phys. 27, 486 (1978)].

[26]G. G. Volkov *et al.*, Yad. Fiz. 27, 1608 (1978) [Sov. J. Nucl. Phys. 27, 846 (1978)].

[27]F. Gürsey and D. Sikivie, Phys. Rev. Lett. 36, 775 (1976).

[28]A. Bottino and W. Kim, Phys. Rev. D 18, 3172 (1978).

[29]P. C. Bosetti *et al.*, Phys. Rev. Lett. 73B, 380 (1978).

[30]M. R. Krishnaswamy *et al.*, Phys. Rev. Lett. 57B, 105 (1975).

[31]A. DeRujula, H. Georgi, and S. L. Glashow, Phys. Rev. Lett. 35, 628 (1975).

[32]J. C. Armitage *et al.*, Nucl. Phys. B150, 87 (1979); P. Bhat and P. Murty, Pramana 10, 115 (1978).

[33]B. C. Barish *et al.*, Phys. Rev. Lett. 38, 577 (1977); A. Benvenuti *et al.*, *ibid.* 38, 1110 (1977).

[34]R. M. Barnett and L. N. Chang, Phys. Lett. 72B, 233 (1977); K. Ishikawa, S. Midorikawa, and M. Yoshimura, Prog. Theor. Phys. 59, 227 (1978); V. K. Cung and C. W. Kim, Phys. Lett. 69B, 359 (1977); C. Albright, J. Smith, and J. A. M. Vermaseren, Phys. Rev. Lett. 38, 1187 (1977); P. Langacker and G. Segre, *ibid.* 39, 259 (1977); C. K. Cung, C. W. Kim, and P. Sikivie, Phys. Rev. D 18, 3164 (1978); D. Horn and G. G. Ross, Phys. Lett. 69B, 364 (1977); F. N. Widili and G. C. Chukwumah, Phys. Rev. D 17, 1304 (1978).

[35]D. J. Bechis, C. Y. Chang, and K. H. Lau, Phys. Rev. D 20, 99 (1979); J. Smith, Phys. Lett. 85B, 124 (1979); T. Hansl *et al.*, *ibid.* 77B, 114 (1978); A. Benvenuti *et al.*, Phys. Rev. Lett. 42, 1024 (1979); T. Hansl *et al.*, Nucl. Phys. B142, 381 (1978); C. H. Albright, J. Smith, and J. A. M. Vermaseren, Phys. Rev. D 18, 108 (1978).

[36]W. R. Francis *et al.*, Phys. Rev. Lett. 38, 633 (1977).

[37]J. D. Bjorken and C. H. Llewellyn Smith, Phys. Rev. D 7, 887 (1973).

[38]J. Ellis, in *Weak Interactions—Present and Future*, proceedings Summer Institute on Particle Physics, 1978, edited by Martha C. Zipf (SLAC, Stanford, 1978).

[39]C. G. Callan and D. G. Gross, Phys. Rev. Lett. 21, 311 (1968).

[40]B. A. Gordon *et al.*, Phys. Rev. D 20, 2465 (1979), Table X, Column 3.

[41]This approximation is an empirical fit to data in S. Stein *et al.*, Phys. Rev. D 12, 1884 (1975).

[42]The mass range used is approximately $0.34 m_{M^0} \leq m \leq m_{M^0}$.

[43]The contour outlines the region $(Q^2)^{1/2} > 3.0$ and $p_\perp > 3.44 - 0.11(Q^2)^{1/2}$.

[44]For a description of the determination of the number of J/ψ and ψ' states in the trimuon sample see Chap. VII.

[45]A. Benvenuti, in *Proceedings of the 1979 International Symposium on Lepton and Photon Interactions at High Energies, Fermilab*, edited by T. B. W. Kirk and H. D. I. Abarbanel (Fermilab, Batavia, Illinois, 1979), p. 149. The integrated luminosity is assumed to be the product $(1.5 \times 10^{11}$ muons$) \times (10$ modules$) \times (500$ cm of carbon/module$) \times ($density$=1.55$ g/cm$^3) \times 6 \times 10^{23}$.

[46]J. P. Leveille and T. Weiler, Nucl. Phys. B147, 147 (1979), and references cited therein. In this model the fraction of bound heavy quarks in the 1S state is perhaps best regarded as a fit parameter. In agreement with ψ data (Ref. 47) we use the value $\frac{1}{6}$. See V. Barger, W. Y. Keung, and R. J. N. Phillips, Phys. Lett. 91B, 253 (1980).

[47]T. Weiler, Phys. Rev. Lett. 44, 304 (1980).

[48]B. Niczyporuk *et al.*, Phys. Rev. Lett. 46, 92 (1981). If the bottom quark were to have charge $\frac{2}{3}$, a substantially larger branching ratio would be expected.

[49]A. R. Clark *et al.*, Phys. Rev. Lett. 43, 187 (1979); T. Markiewicz, Ph.D. thesis, University of California at Berkeley, 1981 (unpublished).

[50]See, for example, A. Silverman, in *Proceedings of the International Symposium on Electron and Photon Interactions at High Energies, Liverpool, 1969*, edited by D. W. Braben and R. E. Rand (Daresbury Nuclear Physics Laboratory, Daresbury, Lancashire, England, 1970), Table 2.

[51]W. R. Ditzler *et al.*, Phys. Lett. 57B, 201 (1975).

[52]B. Knapp *et al.*, Phys. Rev. Lett. 34, 1040 (1975); U.

Camerini *et al.*, *ibid.* <u>35</u>, 483 (1975); B. Gittleman *et al.*, *ibid.* <u>35</u>, 1616 (1975); T. Nash *et al.*, *ibid.* <u>36</u>, (1976); W. Y. Lee, in *Proceedings of the International Symposium on Lepton and Photon Interactions at High Energies, Hamburg, 1977* (Ref. 6).

[53]T. Bohringer *et al.*, Phys. Rev. Lett. <u>44</u>, 111 (1980). Owing to lack of information we simply assume that Υ' and Υ'' have the Υ branching ratio.

[54]Strictly speaking, our limit is on the sum $\sum_V \sigma(V)B(V \rightarrow \mu^+\mu^-)$, where V runs over Υ, Υ', and Υ''. The Υ' and Υ'' assumptions cited in the text would then lead to a limit on Υ production which is 36% stronger than the limit we have quoted.

[55]G. Aubrecht and W. Wada, Phys. Rev. Lett. <u>39</u>, 978 (1977), make photoproduction predictions which, with γGF ν- and Q^2-dependence assumptions, correspond to 0.15×10^{-36} cm^2 of Υ muoproduction at 209 GeV.

[56]N. Bralic, Nucl. Phys. <u>B139</u>, 433 (1978), makes leptoproduction predictions which, with γGF energy-dependence assumptions, correspond to 0.07×10^{-36} cm^2 of Υ muoproduction at 209 GeV.

[57]H. Fritzsch and K. Streng, Phys. Lett. <u>72B</u>, 385 (1978), make photoproduction predictions which, with γGF ν- and Q^2-dependence assumptions, correspond to 0.36×10^{-36} cm^2 of Υ muoproduction at 209 GeV.

[58]A. R. Clark *et al.*, Phys. Rev. Lett. <u>45</u>, 682 (1980).

[59]K. Chadwick *et al.*, Phys. Rev. Lett. <u>46</u>, 88 (1981).

[60]P. A. Rapidis *et al.*, Phys. Lett. <u>85B</u>, 507 (1979).

[61]We use the decay matrix elements of I. Hinchcliffe and C. H. Llewellyn Smith, Nucl. Phys. <u>B114</u>, 45 (1976).

[62]J. Kirkby, Phys. Rev. Lett. <u>45</u>, 329 (1980).

[63]B. A. Gordon *et al.*, Phys. Rev. D <u>20</u>, 2645 (1979).

[64]W. A. Loomis *et al.*, Phys. Rev. D <u>19</u>, 2543 (1979).

[65]J. A. Gaidos *et al.*, Nucl. Phys. <u>B23</u>, 10 (1973); P. Bosetti *et al.*, *ibid.* <u>B54</u>, 141 (1973); P. Bosetti *et al.*, *ibid.* <u>B60</u>, 307 (1973); G. A. Akopdjanov *et al.*, *ibid.* <u>B75</u>, 401 (1974); W. Morris *et al.*, Phys. Lett. <u>56B</u>, 395 (1975).

[66]The polynomial is $1.0 - 7.56y + 19.81y^2 - 21.79y^3$ $+ 8.66y^4$.

[67]F. J. Gilman, Phys. Rev. <u>167</u>, 1365 (1968).

[68]J. P. Leveille and T. Weiler, Nucl. Phys. <u>B147</u>, (1979).

[69]V. Barger, W. Y. Keung, and R. J. N. Phillips, Phys. Rev. D <u>20</u>, 630 (1979).

[70]H. Fritzsch and K. H. Streng, Phys. Lett. <u>72B</u>, 385 (1978).

[71]J. Babcock, D. Sivers, and S. Wolfram, Phys. Rev. D <u>18</u>, 162 (1978).

[72]D. Horn, Phys. Lett. <u>73B</u>, 199 (1978).

[73]J. Ellis *et al.*, Nucl. Phys. <u>B131</u>, 285 (1977).

[74]M. A. Shifman, A. I. Vainshtein, and V. I. Zakharov, Phys. Lett. <u>65B</u>, 255 (1978).

[75]B. Margolis, Phys. Rev. D <u>17</u>, 1310 (1978).

[76]A. R. Clark *et al.*, Phys. Rev. Lett. <u>45</u>, 682 (1980).

[77]G. D. Gollin *et al.*, Phys. Rev. D <u>24</u>, 555 (1981).

[78]A. G. Frodeson, O. Skjeggestad, and H. Tofte, *Probability and Statistics in Particle Physics* (Universitesforlaget, Norway, 1979), pp. 424—428.

[79]F. J. Massey, J. Am. Stat. Assoc. <u>46</u>, 68 (1951); Z. W. Birnbaum, *ibid.* <u>47</u>, 425 (1952).

[80]W. Y. Keung, thesis, University of Wisconsin, 1980 (unpublished).

[81]A. R. Clark *et al.*, Phys. Rev. Lett. <u>43</u>, 187 (1979).

[82]F. J. Gilman, Phys. Rev. <u>167</u>, 1365 (1968).

[83]M. Strovink *et al.*, in *Proceedings of the 1979 International Symposium on Lepton and Photon Physics at High Energies, Fermilab* (Ref. 45), p. 135.

[84]V. Ganapathi and J. Smith, Phys. Rev. D <u>20</u>, 2213 (1979).

[85]V. Ganapathi and J. Smith, Phys. Rev. D <u>23</u>, 75 (1981).

[86]V. Barger, T. Gottschalk, and R. J. N. Phillips, Phys. Rev. D <u>19</u>, 92 (1979).

[87]M. Holder *et al.*, Phys. Lett. <u>70B</u>, 393 (1977).

[88]M. Holder *et al.*, Phys. Lett. <u>73B</u>, 105 (1978).

[89]R. J. Loveless *et al.*, Phys. Lett. <u>78B</u>, 505 (1978).

[90]V. Barger, W. Y. Keung, and R. J. W. Phillips, Phys. Rev. D <u>20</u>, 630 (1979).